

Mountain permafrost in the Central Pyrenees: insights from the Devaux ice cave

Miguel Bartolomé^{1*}, Gérard Cazenave², Marc Luetscher³, Christoph Spötl⁴, Fernando Gázquez^{5,6}, Ánchel Belmonte⁷, Alexandra V. Turchyn⁸, Juan Ignacio López-Moreno¹, Ana Moreno¹

¹ Departamento de Procesos Geoambientales y Cambio Global, Instituto Pirenaico de Ecología-CSIC, Zaragoza, Spain.

² Société de Spéléologie et de Préhistoire des Pyrénées Occidentales (SSPPO), 5 allée du Grand Tour, 64000 PAU, France

³ Swiss Institute for Speleology and Karst Studies (SISKA), La Chaux-de-Fonds, Switzerland

⁴ Institute of Geology, University of Innsbruck, 6020 Innsbruck, Austria

⁵ Water Resources and Environmental Geology Research Group, Department of Biology and Geology, University of Almería, Almería, Spain.

⁶ Andalusian Centre for the Monitoring and Assessment of Global Change (CAESCG), University of Almería, Almería, Spain.

⁷ Sobrarbe-Pirineos UNESCO Global Geopark. Boltaña. Spain.

⁸ Godwin Laboratory for Palaeoclimate Research, Department of Earth Sciences, University of Cambridge, Cambridge, UK

*Correspondence: Miguel Bartolomé (mbart@ipe.csic.es)

Abstract (250 words)

Ice caves are one of the least studied parts of the cryosphere, particularly those located in inaccessible permafrost areas at high altitudes or high latitudes. We characterize the climate dynamics and the geomorphological features of Devaux cave, an outstanding ice cave in the Central Pyrenees on the French-Spanish border. Two distinct cave sectors were identified based on air temperature and

geomorphological observations. The first one comprises well-ventilated galleries with large temperature oscillations likely influenced by a cave river. The second sector corresponds to more isolated chambers, where air and rock temperatures stay below 0°C throughout the year. Seasonal layered ice and hoarfrost occupy the first sector, while transparent, massive perennial ice is present in the isolated chambers. Cryogenic calcite and gypsum are mainly present within the perennial ice. During winter, the cave river freezes at the outlet, resulting in a damming and back-flooding of the cave. We suggest that relict ice formations record past damming events with subsequent formation of congelation ice. $\delta^{34}\text{S}$ values of gypsum indicate that the sulfate originated from the oxidation of pyrite present in the bedrock. Several features including air and rock temperatures, the absence of drips, the small loss of ice in the past seven decades, and the location of ice bodies in the cave indicate that the cave permafrost is the result of a combination of undercooling by ventilation and diffusive heat transfer from the surrounding permafrost, reaching a thickness of ~200 m.

Keywords: Ice cave, cave monitoring, cryogenic cave carbonates, cryogenic gypsum, Pyrenees.

1. Introduction

Mountain areas are among those environments most affected by current climate change ([Hock et al., 2019](#)). In the mid-latitudes, high-altitude areas are subject to mountain permafrost, a very sensitive and unstable phenomenon that responds quickly to environmental changes ([Harris et al., 2003](#); [Biskaborn et al., 2019](#)) due to the number of factors. Snow cover distribution and thickness, topography, water availability, and surface and rock temperature influence the spatial distribution of mountain permafrost ([Gruber and Haeberli, 2009](#)). In light of these processes, multidisciplinary studies including, among others, measurements of rock temperature in boreholes and bottom temperatures of snow cover (BTS), geophysical techniques, and detailed mapping (geomorphology, thermal) are needed to gain a comprehensive understanding of mountain permafrost (e.g. [Lewkowicz and Ednie, 2004](#); [Serrano et al., 2019](#); [Biskaborn et al., 2019](#)). On the other hand, integrated studies of paleo-permafrost (e.g. [Vaks et al., 2020](#)) and modern permafrost, specifically mountain permafrost (e.g., [Supper et al., 2014](#);

[Scandroglio et al., 2021](#)), shed light on past, present and future developments of permafrost areas, an issue of vital importance in the context of global warming. Studies of past permafrost require sedimentary records, which are locally preserved in caves located at high altitudes and/or high latitudes. Temporal and spatial changes in past permafrost distribution have been identified using speleothems (stalagmites, flowstones) in high-latitude and polar regions (e.g., [Vaks et al., 2013, 2020](#); [Moseley et al., 2021](#); [Li et al., 2021](#)) as well as in mid-latitude regions (e.g., [Lundberg and McFarlane, 2007](#); [Fankhauser et al., 2016](#); [Lechleitner et al., 2020](#)).

Ice caves are cavities in rock hosting perennial ice that results from the transformation of snow and/or the freezing of infiltrating water ([Perşoiu and Lauritzen, 2018](#)). Cave ice can be dated and used as a valuable paleoclimate archive in non-polar areas (e.g., [Stoffel et al., 2009](#); [Spötl et al., 2013](#); [Perşoiu et al., 2017](#); [Kern et al., 2018](#); [Sancho et al., 2018a](#); [Leunda et al., 2019](#); [Munroe, 2021](#); [Racine et al., 2022](#)). Recently, coarse cryogenic cave carbonates ($\text{CCC}_{\text{coarse}}$), that form during slow freezing of water inside caves, have been used as indicator of permafrost degradation, permafrost thickness, and subsurface ice formation ([Žák et al., 2004, 2012](#); [Richter et al., 2010a](#); [Luetscher et al., 2013](#); [Orvošová et al., 2014](#); [Spötl and Cheng, 2014](#); [Bartolomé et al., 2015](#); [Dublyansky et al., 2018](#); [Koltai et al., 2020](#); [Munroe et al., 2021](#); [Spötl et al., 2021](#)).

Many ice caves are located in areas where the mean annual air temperature (MAAT) outside the cave is above 0°C ([Perşoiu and Lauritzen, 2018](#)) and, therefore, are highly susceptible to future climate warming ([Kern and Perşoiu, 2013](#)). These ice caves are local thermal anomalies which are controlled by the cave geometry and the associated ventilation pattern. Their ice deposits represent sporadic permafrost occurrences and do not inform about the wider thermal environment. In contrast, at high altitudes and high latitudes subsurface ice deposits are still preserved by the presence of permafrost under the current climate conditions. There, mountain permafrost is limited to areas where a periglacial belt is present, with $\text{MAAT} \leq 0^{\circ}\text{C}$. For example, in the European Alps, discontinuous mountain permafrost is observed above 2600 to 3000 m a.s.l. ([Boeckli et al., 2012](#)), while in southern Europe permafrost is generally absent

(i.e. not observed even on the highest massif of the Iberian Peninsula, [Gómez-Ortiz et al., 2019](#)). In the Central Pyrenees few studies suggest the possible presence of permafrost above 2750 m a.s.l. ([Serrano et al., 2019, 2020](#); [Rico et al., 2021](#)), and the presence of a few ice caves has only recently been documented (e.g. [Sancho et al., 2018a](#); [Serrano et al., 2018](#)) informing about the occurrence of sporadic permafrost.

The aim of this study is to characterize the permafrost conditions in Devaux cave, a high-altitude ice cave in the Central Pyrenees. We monitored air, water and rock temperatures and used cryogenic cave deposits to i) document the distribution of permafrost within this cave, and ii) to study the processes that resulted in perennial cave ice bodies and associated cryogenic mineral occurrences.

2. Study site

Devaux cave opens at ~2838 m a.s.l. in the NE cliff of Gavarnie cirque (France) of the Monte Perdido massif (MPm) in the Central Pyrenees (Fig. 1a). The cave is located between the Parc National des Pyrénées (France) and the Parque Nacional de Ordesa y Monte Perdido (Spain). Named after Joseph Devaux who discovered and explored it in 1928, the cave was later investigated with respect to its hydrogeology and microclimatology and preliminary descriptions of its deposits were reported (e.g., [Devaux, 1929; 1933](#); [Rösch and Rösch, 1935](#); [Rösch, 1949](#); [du Cailar and Dubois, 1953](#); [Requirand, 2014](#)).

The area is dominated by limestones and dolostones ranging from the Upper Cretaceous to the Eocene-Paleocene. MPm is the highest limestone karst area in Europe reaching up to 3355 m a.s.l. (Monte Perdido peak) (Fig. 1b). The nearest peaks to Devaux cave are Marboré (3248 m a.s.l.) and the three Cascada peaks (3164 m, 3111 m, and 3098 m a.s.l.). The limestone thickness above the cave varies between ~200 and 250 m (Fig. 2a). In Devaux, the galleries follow the axis of a NW-SE striking syncline (Fig. 1b). A river runs along the cave (Fig. 2a, b). The cave has two known entrances: the lower one corresponds to the main outlet of the cave river (Brulle spring, North 1, ~2821 m a.s.l.), while the

upper entrance is known as the “Porche” (South, ~2836 m a.s.l.) (Figs. 1c and 2b). Between these two entrances, a small gallery (Spring North 2) opens +1.2 m above Brulle spring (Fig. 1c). Brulle is one of the main springs in the Gavarnie cirque. This spring drains a catchment of ~2.6 km² (polje) located on the southern face of MPm between ~2850 and 3355 m a.s.l. (Figs. 1b and, 1d). Major water flow is observed during late spring and early summer when snowmelt occurs in a catchment characterised by shafts, sinkholes and small closed depressions (Fig. 1d). The water of Brulle spring feeds, together with some other springs located a few hundred meters below, the Gavarnie waterfall (Fig. 1b). A tracer experiment (du Cailar et al., 1953) indicated that part of the water of the Gavarnie waterfall, and thus likely also from Brulle spring, comes from a ponor in the Lago helado (lake, Fig. 1e) located ~2.3 km to the east of Devaux cave (Figs. 1b and 2a). The Gavarnie waterfall (Fig. 1b) turned green within ~21 hours after injection of the tracer but the water at Brulle spring was not directly checked (du Cailar et al., 1953). During the colder months, the spring as well as the Gavarnie waterfall freeze.

The geomorphology of the area is dominated by karst, glacial and periglacial landforms. The area was strongly glaciated during the last glacial period on both sides of the massif (e.g., Reille and Andrieu, 1995; Sancho et al., 2018b; Bartolomé et al., 2021). Today, only two glacier relicts covered by scree deposits are present in the Gavarnie cirque (Fig. 1b): 1) the Cascada dead-ice which is located several hundred meters below Devaux cave, and 2) a dead-ice accumulation in the NE wall of the cirque. Till present close to Brulle spring, on the access to Devaux and in the Cascada glacier, point to a much larger glacier extent in the past, maybe corresponding to the Little Ice Age or even the Neoglacial advance recognized in the nearby Tucarroya (Fig. 1b) and Troumouse cirques (Gellatly et al., 1992; González Trueba et al., 2008; García-Ruiz et al., 2014, 2020).

The study area lies at the transition between Atlantic and Mediterranean climate, with generally cold and dry winters and warm and dry summers. In MPm, the annual 0°C isotherm is located at ~ 2900 m a.s.l. (López-Moreno et al., 2016; Serrano et al., 2019). The wet seasons are fall and spring. The annual precipitation at the Góriz meteorological station (2150 m a.s.l. and 3 km SE of the

cave) averages 1650 mm. However, mass balance calculations of the nearby Monte Perdido glacier, where more than 3 m of snow (density 450 kg/m³) accumulates between November to April, indicates a minimum amount of 1500 mm water equivalent, therefore the total annual precipitation in high parts of the massif exceeds 2500 mm (López-Moreno et al., 2019). In the MPm, discontinuous permafrost is present between ~2750 and ~2900 m a.s.l. and becomes more frequent above ~2900 m a.s.l. on the northern side (Serrano et al., 2019). Periglacial activity is characterized by rock glaciers, solifluction lobes and patterned ground (Feuillet, 2011).

3. Material and methods

3.1 Cave survey and mapping

A survey of Devaux cave was conducted using a compass and clinometer as well as a laser distometer (Disto-X, Heeb, 2014). In addition to cave ice, chemical and clastic deposits were mapped in the cave (Fig. 2b). The labelling of the cave chambers (A to K) follows the nomenclature introduced by Devaux (1929) and Rösch and Rösch (1935).

A map of potential solar radiation (RAD) of the MPm was obtained using an algorithm which considers the effects of the surrounding topography on shadowing considering the position of the sun. RAD was calculated for every month and was then averaged to obtain an annual mean. Details of this computation can be found in Pons and Ninyerola (2008).

3.2 Cave monitoring

The cave consists of large rooms (e.g., room F, and those located beyond SCAL chatière) connected by small galleries (Fig. 2b), locally with narrow passages (e.g., galleries close to SPD room or SCAL chatière, Fig. 2b). 15 stations were installed in the outmost ~350 m of the cave to monitor air (11 sensors), water (2 sensors) and rock temperature (2 sensors) (Fig. 2b). Cave air temperature variations were recorded using different devices (Hobo Pro v2 U23-001 (accuracy ±0.25°C, resolution 0.02°C), Tinytag Talk 2 (accuracy ±0.5°C, resolution, 0.04°C) and ELUSB2 (accuracy ±0.21°C, resolution 0.5°C)). The cave river temperature

was recorded at two points. The first site (W7) was located close to the Brulle spring (Fig. 2b; Hobo TiDBit V2, accuracy $\pm 0.21^{\circ}\text{C}$, resolution 0.02°C) and, the second site (W6) was located in room F (Fig. 2b; Hobo UA-001-08; accuracy $\pm 0.53^{\circ}\text{C}$, resolution 0.4°C). Both sensors were installed at a water depth of 20 cm. Finally, the rock temperature was recorded at two sites (R1 and R2 in room D and K, respectively) using a Hobo U23-003 device (accuracy $\pm 0.25^{\circ}\text{C}$, resolution 0.02°C). Each sensor has two external temperature probes (channels 1 and 2, Ch1-Ch2). These temperature probes were installed in two horizontal drill holes of 60 cm depth, ~ 1.5 to 2 m from each other.

We monitored sporadically the cave during different intervals between 2011 and 2015, while a continuous monitoring was carried out between July 2017 and July 2021. Maximum, minimum and mean temperatures as well as the number of frost/warm days were obtained for each sensor and site (Fig. 2b). Changes in the ice morphology were evaluated using wall marks measured at four points since 2013 in room G and using one point during 2020-2021 in room SPD (Fig. 2b) using a digital sliding caliper.

The outside temperature was measured at the “Porche” entrance (~ 2836 m a.s.l.) and on the southern face of MPM at ~ 2690 m a.s.l. For comparison, these temperature records were corrected assuming an adiabatic lapse rate of $5.5^{\circ}\text{C km}^{-1}$ (López-Moreno et al., 2016; Navarro-Serrano et al., 2018) to an elevation of ~ 2850 m a.s.l., corresponding approximately to the lower limit of the hydrological catchment area of Devaux. In both cases, the temperature was measured using Tinytag Talk 2 sensors equipped with a radiation shield. These data were compared to the temperature record from the Pic du Midi de Bigorre meteorological station (PMBS; 2011-2020) (2860 m a.s.l., ~ 28 km N of Devaux) obtained from Météo-France. Moreover, the homogenised data available since 1882 from PMBS (Bücher and Dessens, 1991; Dessens and Bücher, 1995) were used to identify long-term temperature trends.

3.3 X-ray diffraction, ion chromatography and sulfur isotopes

X-ray diffraction (XRD) analyses were performed on sulfate and carbonate crystals from rooms G, D and K, as well as on sulphide and oxidized crystals thereof from the host rock (Fig. S1). The analyses were performed at the

Geosciences Institute in Barcelona (GEO3-BCN-CSIC) using a Bruker-AXS D5005 powder diffractometer configured in $\theta/2\theta$ -mode (e.g. [Rodríguez-Salgado et al., 2021](#)).

Samples of cave drip water, ice and river water were analysed for major ions by ion chromatography (IC) at the laboratories of the Pyrenean Institute of Ecology (Zaragoza). Carbonate alkalinity was determined by titration within 24 hours after sampling.

Sixteen samples, including sulfate crystals, dissolved sulfate and pyrite crystals were selected for sulfur isotope analysis at the Godwin Laboratory for Paleoclimate Research of the University of Cambridge (UK), following the methodology of [Giesemann et al., \(1994\)](#). For gypsum samples, ~5 mg of powdered gypsum were dissolved in deionized water at 45°C overnight. Then, a BaCl₂ solution (50 g/L) was added to induce BaSO₄ precipitation. In the case of water samples, BaCl₂ was added directly to the sample. Subsequently, 6M HCl was added to remove any co-precipitated carbonate minerals and the BaSO₄ precipitate was rinsed several times with deionized water. Finally, BaSO₄ was dried at 45°C overnight. Sulfate dissolved in water were precipitated using the same method.

Isotope measurements were carried out using a Flash Elemental Analyzer (Flash-EA) at 1030 °C. The samples were folded in tin capsules. After sample combustion, the generated SO₂ was measured by continuous-flow gas source isotope ratio mass spectrometry (Thermo Scientific, Delta V Plus). Samples were run in duplicate and calibration was accomplished using NBS-127. The reproducibility (1σ) of $\delta^{34}\text{S}$ was better than 0.2‰, similar to the long-term reproducibility of the standard over the run (0.2‰). $\delta^{34}\text{S}$ isotope values are reported relative to VCDT (Vienna-Canyon Diablo Troilite).

4. Results

4.1 Devaux cave description

Devaux cave is ~2500 m long and comprises three distinct levels (Fig. 2b). The lower and the middle levels correspond to the Brulle spring (0 m), and the “Porche” entrance (~+14.5 m), respectively. The third one comprises chambers

and galleries +21 m to +29 m above the Brulle spring (Fig. 2b). In the inner part of the cave, some unexplored vertical chimneys may connect to sinkholes in the catchment above the cave (Fig. 2a). The main ice deposits are located in rooms D, G, SPD and K (Fig. 2b). Except for SPD, these chambers located above the Porche entrance (between ~+1 and +7 m) can be accessed via ascending passages.

During the cold season, the cave river starts freezing at the spring and the ice then expands backward into room F (Fig. 2b). The ice totally or partially clogs the main gallery and dams the water inside the cave forming a small lake (cf. also [Rösch and Rösch, 1935](#)). This process is important for the seasonal ice extent as the flooding of the cave depends on whether the springs (North 1 and North 2) are frozen or not (e.g., [Rösch and Rösch, 1935](#)). Webcam observations (Gavarnie, Oxygène hut) suggest a possible freezing of the Brulle spring from late November to mid-May simultaneous with the freezing of the Gavarnie waterfall. Moreover, historical photos (e.g., [Devaux, 1929](#); [Rösch and Rösch, 1935](#)) and our own observations show that snow during winter and spring can reach the Brulle entrance - a situation that also favours the blocking of the springs. As a result of such flooding events, slackwater deposits formed in the cave entrance zone, but locally also further into the cave (e.g., in rooms I, J, K and SCAL chatière, along the main gallery; Fig. 2b), while silty sediments are found at elevated positions with respect to the river level (e.g., in rooms D and G). Sandy sediments dominate in the large rooms located beyond the SCAL chatière. Two such successions (~1 m thick) comprising hundreds of rhythmic fine sand and silt layers are present in elevated areas with respect to the current river, witnessing major events of back-flooding.

Observations made during summer show a dominant air-flow direction from the inner to the outer parts of the cave, exiting through the Brulle and Porche entrances. Conversely, the opposite is expected for the cold season (chimney effect). When the Brulle spring is partially clogged by ice during early summer forcing the stream to flow below the ice, air flows from room F to C (Fig. 2b) (e.g., summer 2021). The air flow is imperceptible in rooms D, G, and close to K located away from the main cave passages.

4.2 Climate setting of Devaux cave

The MAAT at the elevation of Devaux cave is $\sim 0^{\circ}\text{C}$ (-0.04°C ; 2017-2021). On the other hand, a positive MAAT (1.8°C) is recorded on the southern side of the MPm at a similar altitude (Fig. 3a). Maximum and minimum air temperatures outside the cave vary between 24.5°C and -17.2°C (hourly values, 2017-2021). The PMBS MAAT record (Fig. 3b) shows a warming trend of around $+1.5^{\circ}\text{C}$ since the beginning of the measurements in 1882. Before 1985, temperatures below 0°C dominated the annual cycle, while positive MAATs became more frequent in recent years. Minimum temperatures also show an increasing trend of $\sim +2.5^{\circ}\text{C}$, while the maximal annual temperatures do not show a clear trend. The north-facing Gavarnie cirque is associated with a clear RAD anomaly (Fig. 4). Values lower than 215 kWh/m^2 are observed at $\sim 2000\text{ m}$ and between ~ 2800 and 2900 m a.s.l. , corresponding to the cirque bottom, the area located behind La Torre peak and the surroundings of Devaux cave. At the cave entrance the RAD value is only 390 kWh/m^2 , in stark contrast to the summit areas and surroundings where the RAD often exceeds 1500 kWh/m^2 (Fig. 4).

While the mean daily air temperature (MDAT) at the cave entrance (purple line in Fig. 5) and the temperature series from PMBS (pink line in Fig. 5) agree in their absolute values, the variability of MDAT at the Devaux entrance is lower than at the PMBS. This pattern could be related to local topographic conditions leading, for instance, to less RAD, or to the position of the sensor in the cliff (less night emissivity). Given this radiation contrast, warmer temperatures prevail on the southern side of the MPm (Fig. 4), favouring early snowmelt in spring and early summer, while at the same time the temperature stays below 0°C in the cave's surroundings.

4.3 Devaux cave temperature variations

The cave can be separated into distinct areas depending on their thermal regime: ventilated galleries (rooms A, B, C, F and the main gallery from SPD to SCAL chatière)) and poorly ventilated parts off the main air flow path (rooms D, G, K - Figs. 2b, 5).

4.3.1 Well-ventilated cave parts

Air ($T_{2\text{air}}$, $T_{5\text{air}}$, $T_{10\text{air}}$, $T_{11\text{air}}$) and water ($W_{6\text{water}}$, $W_{7\text{water}}$) temperature data show large seasonal oscillations. All sensors except $T_{11\text{air}}$ show a few days of positive temperatures during summer. Sensor $T_{2\text{air}}$ (2011-2012, Fig. 5a), which is also the closest to the Porche entrance, shows the highest correlation (r) with the external temperature (0.73, $p < 0.001$). Sensor $T_{5\text{air}}$ (2017-2021, Fig. 5d) in room B also shows a high correlation and significant correlation (0.82, $p < 0.0005$) with the outside temperature. During the major cave cooling that takes place between the end of October and May and the correlation is significant and ranges between 0.68 to 0.84. During summer and part of fall, the correlation decreases notably (-0.23 to 0.76). Sensor $T_{11\text{air}}$ (2018-2021, Fig. 5d) is partly protected from the air flow and shows lower a correlation (0.69, $p < 0.001$) despite being located in a well-ventilated gallery (SPD room). Also during the winter months, the correlations are lower (0.49-0.62, $p < 0.001$) than in $T_{5\text{air}}$. Sensor T_{10} (2014-2015, Fig. 5c) does not show any significant correlation with the external temperature.

Sensors $W_{6\text{water}}$ and $W_{7\text{water}}$ (Figs. 5b, c) recorded water temperature variations during the years 2012-2013 and 2014-2015, respectively. Both sensors record a continuous temperature decline from the end of November to mid-January until the water freezes. At $W_{7\text{water}}$, the temperature ranges between -0.3 and -5.8 °C between the end of fall and the beginning of winter, while the temperature stays close to 0°C between January and the beginning of June. At $W_{6\text{water}}$, the temperature reached a minimum of -1.7 °C and shows smaller variations than at $W_{7\text{water}}$. No significant correlation was found between the external air temperature and the river water temperature. Only $W_{6\text{water}}$ shows a weak correlation with the external temperature when ice is absent (0.39 $p < 0.001$ and 0.40 $p < 0.001$).

For each monitored interval, the mean annual cave temperature at the $T_{2\text{air}}$, $T_{5\text{air}}$ and $T_{11\text{air}}$ sensors is lower than the outside mean temperature (by 0.4°, 2.0°, 3.3° C, respectively). The $W_{6\text{water}}$, $W_{7\text{water}}$ and $T_{10\text{air}}$ sensors show mean temperatures higher than the external mean temperatures (by 1.6°, 2.6°, 2.5° C, respectively). The periods 2011-2012 and 2017-2018 (at $T_{2\text{air}}$ and $T_{5\text{air}}$, respectively) represent the coldest cave years of the monitoring period.

4.3.2 Poorly ventilated cave parts

Sensors located in rooms D ($T_{3\text{air}}$, $T_{4\text{air}}$, $T_{8\text{air}}$), G ($T_{9\text{air}}$), K ($T_{12\text{air}}$) and rock temperature ($R_{1\text{rock}}$, $R_{2\text{rock}}$) show air temperatures below 0 °C during the monitoring period with small oscillations and a weak and/or insignificant correlation with the external air temperature. Sensor $R_{1\text{rock}}$ (Fig. 5) recorded rock temperatures consistently below 0°C during the entire monitoring period. This sensor shows constant rock temperatures (-1.24 °C and -1.27 °C for channels 1 and 2, respectively), similar within error to the cave air temperature ($T_{3\text{air}}$, $T_{9\text{air}}$; 2019-2021). All sensors except for $T_{3\text{air}}$ (2011-2012, Fig. 5a) show mean air and rock temperatures lower than the mean external temperature during the same period (by 0.59 °C to 2.47°C). The muted temperature variations in these chambers reflect reduced heat exchange compared to the well-ventilated parts of the cave. Sensors $T_{12\text{air}}$ and $R_{2\text{rock}}$ are located in room K, and similar to $T_{11\text{air}}$, the chamber morphology shields them from the air flow. Rock temperature sensor $R_{2\text{rock}}$ shows a slightly more variable temperature ranging between -0.19°C and -0.28°C (mean of -0.24 and -0.23°C for channel 1 and 2, respectively). Sensor $T_{12\text{air}}$ shows a low correlation with the external temperature ($r^2=0.35$, $p<0.001$ (2018-2021)), and the same is observed for T_{ext} - $R_{2\text{rock}}$ ($r^2=0.35$, $p<0.001$ (2019-2021)). Meanwhile the correlation between $T_{12\text{air}}$ and $R_{2\text{rock}}$ is high but not significant ($r^2=0.93$, $p>0.005$ (2019-2021)).

4.4 Cave deposits

4.4.1 Ice

Congelation ice formed by freezing of water within the cave is the most abundant type of ice, and four main ice deposits are located in chambers D, G, SPD, and K (Fig. 2b). The most relevant feature of these ice bodies is their high transparency and massive aspect, i.e. the lack of layering (Figs. 6a, b). Transparent ice is present on the ceiling, blocking chimneys, galleries and fractures. The local loss of transparency is related to the presence of cryogenic cave minerals and/or air inclusions (Figs. 6a, b, c, d).

A highly transparent ice deposit covers the southwest wall of room D and blocks the access to a gallery (Fig. 6a). The height of this deposit reaches ~6 m, and its base is located ~20 m above the Brulle spring. The thickness of this ice deposit ranges from 4.5 to 14.5 m (horizontal laser measurements across the ice in the gallery blocked by ice) and the estimated volume ranges from ~350 to ~710 m³. Three unconformities marked by cryogenic minerals were identified in this ice body.

In room G, an ice body (~25.8 to 29.6 m above the Brulle spring) is present on the ceiling (Fig. 6b) and the estimated ice volume is ~180 m³. A comparison with a historical photograph shortly before 1953 ([Casteret, 1953](#)) suggests that the ice body has not changed significantly during the last ~69 years (Figs. 7a, b). Ice-rock distances measured at four points, however, reveal small changes at three of them. The first has retreated 9.8 mm since 2014 (mean 0.9 mm a⁻¹, n=2), the second has retreated 19.2 mm since 2014 (mean 0.6 mm a⁻¹, n=5), and the third one has retreated 15.8 mm since 2013 (mean 2.2 mm a⁻¹, n=7). At ~80 m from the entrance, a small descending room (SPD) (Figs. 2b, 6c) hosts a small volume of ice. Measurements between 2020 and 2021 indicate a retreat of 20 mm a⁻¹ (n=1). A last major ice deposit is present ~280 m from the entrance (room K), where transparent and massive ice (~15.5 m above the Brulle spring) currently fills a cupula or chimney (Figs. 2b, 6d). Additional ice bodies are present behind the SCAL chatière in the upper gallery (Fig. 2b), but they have not been studied.

In contrast to these massive ice deposits, layered ice of seasonal origin is present in small chambers adjacent to the river (E and F rooms) (Fig. 6e). This ice forms sheets of about 10-15 cm in thickness which are present in room F and nearby areas (Fig. 6f). This ice is related to the damming and freezing of water inside the cave when the Brulle spring freezes. Our visits from 2017 to 2021 revealed that most of the damming and subsequent ice formation in room F took place during winter and spring 2017-2018 corresponding with the coldest months (both inside the cave and outside) of the monitoring period (Fig. 5d). These ice slabs are characterized by flat surfaces on both sides and obviously record incomplete freezing of the dammed water. The ice sheets largely disappeared during summer and fall, and only strongly degraded ice remained in elevated areas of room F.

On the other hand, ice sheets associated with earlier episodes of river damming and freezing have disappeared, and only linear colour changes remained as witnesses of such events on the walls of the room E (Fig. 8d). A historical photograph exemplifies these ice levels in the access between rooms F and E (Fig. 8a). In August 1984 the ice was close to the ceiling and nearly 1 m thick (Fig. 8a; Marc Galy, pers. comm.). This contrasts with the low ice level in recent years (Fig. 8b). In total, three ice-level marks were identified in relation to back-flooding and subsequent freezing of ponded water (Figs. 8c, d). They appear at a lower elevation than the Porche entrance (c.+9.5, +9.2, +8.8, m with respect to the Brulle spring).

Another important feature is the presence of hoarfrost, which was observed in room A, B, F and along the gallery between SPD and J (Figs. 2b, 7g, h). The crystal size varies from few mm to 4 cm and appears to be upholstering some galleries and cupolas, forming aggregates that hang from the ceiling (Fig. 6h). Finally, seasonal ice formations (e.g., icicles and ice stalagmites), as well as drips are restricted to the outmost ~15 m, in the vicinity of both entrances, and in the innermost part of the cave (~ 500 m from the entrance). Seasonal ice formations are absent in cave sectors where transparent ice bodies and hoarfrost are present. Firn deposits derived from snow are restricted to the Porche entrance.

4.4.2 Mineral deposits

They comprise mainly cryogenic cave minerals. XRD analyses of samples from rooms D, G and K yielded gypsum and calcite, while the sulfide crystals and their oxidation products present in the host rock were identified as pyrite and goethite, respectively. The presence of cryogenic gypsum in Devaux was already reported by [du Cailar and Dubois \(1953\)](#). In room D, gypsum was observed within the ice and on boulders (Figs. 9a, b, c). A total of three gypsum levels (lower, middle and upper, located at ~21.4, ~22.6 and ~23.9 m, respectively, with respect to the Brulle spring) were identified in the ice (Fig. 9a). Due to the progressive retreat of the ice body, some of these crystals are now present on the ice surface. Gypsum levels comprise large single crystals (0.5-1 cm in diameter), aggregates forming rafts (10 cm) up to 1 cm in thickness (Fig. 9b), as well as a fine crystalline fraction. Examination of the fine fraction using a binocular stereo microscope indicates the

presence of cryogenic cave carbonates and gypsum (CCG) including globular, single and twin morphologies <1 mm in diameter (Fig. 9d).

In room G, gypsum and carbonates crystals are present in the lower part of the ice deposit (Fig. 10e) and on blocks. There, CCC are larger (>10 mm) than in room D and include globular shapes and raft-like aggregates, similar to those reported by Žák et al. (2012). Some of these CCC show gypsum overgrowths (Fig. 9f). Across the ice surface, patches of globular CCC (sub-millimetre size) have been released by ice sublimation (Figs. 7a, b). In room SPD, CCC and CCG (≤ 2 mm) are present within and on the ice (Figs. 2b, 7c). Finally, in room K, only few CCC were still present within the ice, while most of them form heaps of loose crystals covering blocks. Some of these CCC exceed 5 mm in diameter. Crystal morphologies include rosettes, skeletons and rhombohedrons similar to those reported by Žák et al. (2012) as well as white tapered crystal aggregates. Beyond room K, regular carbonate speleothems (i.e. stalagmites, stalactites and flowstones) are present. Gypsum coating walls or ceilings was not observed.

4.5 Cave water chemistry and sulfate isotopic composition

The chemical composition of water in Devaux cave is dominated by calcium and bicarbonate with relatively high Mg concentrations and locally also elevated sulfate concentrations (Table 1). Total dissolved solids (TDS, $n=7$) vary from 57 to 315 mg l⁻¹. Devaux's dripwater has higher mean sulfate concentrations (65 mg l⁻¹) than the cave river (11 mg l⁻¹) and massive and seasonal ice (2.8-18 mg l⁻¹). The $\delta^{34}\text{S}$ value of dissolved sulfate in the dripwater is -14.4‰ ($n=1$), which is significantly higher than in cave river water (-28.5‰ to -27.3‰, $n=2$; Table 2). Gypsum crystals in room D show $\delta^{34}\text{S}$ values ranging from -15.1‰ to -15.8‰ ($n=7$), while in room G they range from -12.3‰ to -11.9‰ ($n=5$). A pyrite sample from the host rock yielded a $\delta^{34}\text{S}$ value of -12.7‰ ($n=1$).

5. Discussion

5.1. Processes controlling the thermal regime in Devaux cave and the extent of permafrost

A complex spatial distribution and a high degree of heterogeneity are among the main characteristics of mountain permafrost (Gruber and Haeberli, 2009). In Devaux cave the existence of permafrost can be related to a combination of two processes: i) cave atmospheric dynamics, and ii) conductive heat transfer through the rock.

Devaux cave is characterized by mean air and rock temperatures lower than the external mean annual temperature (Fig. 5). The low cave temperatures in winter lead to an inward airflow and an associated negative thermal anomaly behind the entrance zone. On the contrary, during summer the cold and dense air flows out of the cave due to the temperature difference between outside and inside air. The heat supplied to the cave by the river also influences the cave air temperature by exporting thermal energy from the cave during winter. Similar seasonal ventilation patterns have been observed in ice caves elsewhere (e.g., Luetscher et al., 2008; Colucci and Guglielmin, 2019; Perşoiu et al., 2021).

On the other hand, positive temperatures are observed both in the cave river and in the air at the entrance (Fig. 5), reflecting heat advected by water (river) and the influence of the external temperature (cf. Luetscher et al., 2008; Badino, 2010). The lack of correlation between the external and internal temperatures and the small temperature variability in rooms D, G, and K reflect their thermal isolation from well-ventilated cave parts. There, the apparent thermal equilibrium between the rock and the cave atmosphere ($T_{\text{rock}}=T_{\text{air}}$) supports the notion that heat exchange is dominated by conduction through the bedrock.

The MAAT at the altitude of the cave is $-0.04\text{ }^{\circ}\text{C}$ (2017-2021) suggesting that the $0\text{ }^{\circ}\text{C}$ isotherm is located close to the cave. Using an array of techniques (geomatic surveys, temperature monitoring, temperature at the base of the snowpack (BTS) and geomorphological and thermal mapping), Serrano et al. (2019) observed mean annual ground temperatures between -1 and $-2\text{ }^{\circ}\text{C}$ on the northern slope of the MPm suggesting that discontinuous permafrost is present between 2750-2900 m a.s.l., with more continuous permafrost starting at 2900 m a.s.l. The orientation of the Gavarnie cirque, as well as the high slope angle, and shadow from the surrounding peaks favour the preservation of permafrost at lower elevations (e.g., Gubler et al., 2011).

Given the high thermal inertia of the rock, the permafrost temperature at depth is still under the influence of past climate conditions (e.g., [Haeberli et al., 1984](#); [Noetzli and Gruber, 2009](#)) and, therefore, part of the current permafrost in the area could be inherited from previous colder times (e.g., [Colucci and Guglielmin, 2019](#)). In particular, the low mean annual temperatures recorded at PMBS in the late 19th century were favourable conditions for permafrost development. We surmise that the current permafrost could be inherited from colder periods of the Little Ice Age.

In well-ventilated ice caves hoarfrost is the most dynamic ice formation on seasonal time scales. The presence of perennial hoarfrost is, however, indicative of a continuously frozen bedrock and thus representative of caves within the permafrost zone (e.g. [Luetscher and Jeannin, 2018](#); [Yonge et al., 2018](#)). In Devaux cave, perennial hoarfrost is observed in rooms where the bedrock is surrounded by small ice bodies (e.g., gallery close to SPD room, Fig. 6g). On the other hand, seasonal hoarfrost is present in ventilated galleries (A, B, C, F and between SPD and J). Seasonal hoarfrost in room B and C, and in the area between H to J, disappears at the end of summer, probably because of the heat delivered by the cave river, as recorded by the T5 sensor (Fig. 5).

The presence of permafrost in Devaux's catchment is supported by the absence of drips and/or seepage in the investigated cave passages (e.g., [Luetscher and Jeannin, 2018](#); [Vaks et al., 2020](#)). Active drips and seasonal ice formations are limited to the first ~15 m of the cave as well as to the inner part (beyond room K). Mountain permafrost thus penetrates ~350 m longitudinally from the eastern cliff of the Gavarnie cirque to the southern side of the massif. On the other hand, given the elevation of the cave and the topography above the cave, the current maximum permafrost thickness on the southern side of the MPm is ~200 m (without taking into account the active layer).

5.2. The origin of ice in Devaux cave

The transparent and massive character of Devaux's cave ice, as well as the presence of CCC, which formation requires low congelation rates ([Žák et al., 2004](#)), suggests that this ice formed by slow freezing of water dammed by ice at the spring. This model is consistent with the climate of the Gavarnie cirque,

cave geomorphological observations, cave air and water temperatures as well as historical reports. The cave water level can rise by several meters as indicated by slackwater deposits upstream of the Brulle spring.

The distribution and characteristics of ice bodies in Devaux cave indicate that the hydraulic head rose by at least ~ 15 - 29 m, which is the elevation of the ice bodies in rooms G, F and K. This situation requires that all springs (including Porche) are blocked for a sufficiently long time to allow for complete freezing of these cave lakes. The lack of important unconformities in this massive ice (e.g., detrital layers), which are usually related to seasonal ablation (e.g., [Luetscher et al., 2007](#); [Stoffel et al., 2009](#); [Hercman et al., 2010](#); [Spötl et al., 2013](#)), suggests that the ice deposit in room G it is the result of a single flood event. On the contrary, the small unconformities recognized in the ice body in room D suggest that several cycles of damming and subsequent ice formation cannot be discarded in the formation of this ice deposit.

These observations indicate that under the current climate (both in the cave and outside) only part of the water dammed in rooms F and E freezes during winter and spring. This strongly suggests that the ice bodies in Devaux cave must have been associated with colder and/or longer events of ponding and freezing than today, when the cave was effectively sealed from the outside for prolonged times. We hypothesize that the advance of a glacier on the steep slopes of Devaux's surroundings could have contributed to the blockage of the spring, leading to backflooding and the formation of large ice bodies in the cave. In the study area, such periods of glacier growth occurred during the Little Ice Age and/or the Neoglacial ([González Trueba et al., 2008](#); [García-Ruiz et al., 2014, 2020](#)).

The freezing of a flooded cave passage cannot be explained by the advection of cold air alone. It is thus surmised that heat transfer through the host rock is a more plausible mechanism for the complete freezing of ponded water. The cave ice bodies as well as the presence of cryogenic minerals therefore record a long cold period or several shorter episodes. Although cryogenic minerals and in particular CCC_{coarse} are typically associated with permafrost thawing during warm

spells (Žák et al., 2004; Richter et al., 2010; Žák et al., 2012; Luetscher et al., 2013), permafrost conditions prevailed during ice formation in Devaux cave. The water that feeds Devaux's springs infiltrated during late spring and summer from ponors at Lago helado and/or surrounding poljes. However, the heat supplied by this water may have probably not been enough to thaw the frozen host rock. It is thus very likely that the hostrock temperature was lower and/or the outlets remained closed for longer periods than today to allow for the complete slow freezing of the ponded water.

5.2.1 Ice volume changes

The colour changes in the walls close to the river (room E), the historical photograph as well as speleological reports point to large changes (several meters) in the height of the seasonal ice in the flood-prone sector of the cave (Figs. 8a, b). This ice is influenced by the heat exchanged between the water and the cave.

In contrast, changes in the ice volume are almost negligible in rooms D and G where the temperature is more constant and below 0°C (Figs. 7a, b). The ice body in room G has been retreating by only ~0.6 to ~2.2 mm a⁻¹. A similar value (3 mm a⁻¹) was observed in Coulthard cave (Alberta, British Columbia, Marshall and Brown, 1974), a cave located in permafrost (Yonge et al., 2018). Changes in the ice body in this cave were related to slow sublimation due to convective air flow inside the cave (Marshall and Brown, 1974). On the other hand, the ice in SPD room shows higher ice retreat rates (~ 20 mm a⁻¹). Similar sublimation rates have been reported in 'ice caves in the Pamir Mountains and the northern part of the Russian Platform (Mavlyudov, 2008; Žák et al., 2018). Overall, Devaux's cave ice deposits show a remarkable stability which contrasts with the rapid changes observed in ice caves outside permafrost areas (Kern and Perşoiu, 2013; Perşoiu et al., 2021; Wind et al., 2022), including other ice caves in the Pyrenees and Picos de Europa (Belmonte-Ribas et al., 2014; Gomez-Lende et al., 2014, 2016).

5.3. Cryogenic cave minerals

In Devaux cave, CCC and CCG are still present within the ice (Figs. 6, a, b, c, d). Worldwide, only very few *in situ* observations of coarse-grained cryogenic cave

minerals are known (e.g., [Bartolomé et al., 2015](#); [Colucci et al., 2017](#)). [du Cailar and Dubois \(1953\)](#) reported the presence of gypsum crystals at ~50 cm depth within the ice in Devaux cave. The first evidence of *in situ* CCC_{coarse} in cave ice was reported from Sarrios 6, an ice cave at 2780 m a.s.l. on the southern slope of the MPm ([Bartolomé et al., 2015](#)). [Colucci et al. \(2017\)](#) documented the presence of CCC_{coarse} in a small ice cave in the Italian Alps. Recently, [Munroe et al. \(2021\)](#) found CCC_{coarse} in ice of Winter Wonderland cave (Utah, USA). Because of the abundance of cryogenic cave minerals, the size of individual crystals and aggregates thereof, and their different mineralogy, Devaux cave provides an additional opportunity for studying the origin of such cryogenic cave minerals.

CCG in Devaux cave represents, to our knowledge, the first occurrence of its kind in a carbonate karst terrain. So far, CCG have only been reported from gypsum karst areas in Russia and Ukraine ([Korshunov and Shavrina, 1998](#); [Žák et al., 2018 and references therein](#)). In those caves, tiny gypsum crystals form during rapid freezing of water. When ice sublimates in winter, these particles are released and accumulate as powdery deposits on the ice surface. Eventually, they partly dissolve during spring and summer due to the increase in cave air humidity, and later recrystallize forming a wide variety of crystal morphologies. CCG from Devaux cave shows features that do not correspond to those previously published from gypsum karst caves. In particular, the Devaux cave CCG i) appears together with CCC_{coarse} crystals (≥ 5 mm in some cases, in rooms D and G), ii) the (raft-like) gypsum crystals are large (Fig. 9b) and, in some cases, are still found within the ice (Fig. 9a) and surrounded by milky ice rich in air inclusions (Fig. 9a, e), and iii) boulders are locally overgrown by gypsum (Fig. 9c).

Coarse-grained cryogenic cave minerals form in a semi-closed system, when water freezes very slowly ([Žák et al., 2004](#)). Once supersaturation is reached, CCM start to crystallize. The formation of gypsum crystals requires the presence of elevated concentrations of dissolved sulfate which may relate to i) sedimentary gypsum deposits intercalated within carbonates (e.g., [Sancho et al., 2004](#)), ii) the presence of hydrothermal water containing H₂S related to hydrocarbons (e.g., [Hill, 1987](#)), or iii) the oxidation of sulfides (e.g., pyrite) disseminated in carbonate

rocks (e.g., [Bottrell, 1991](#)). In the case of Devaux cave marine evaporite rocks (e.g., of the Upper Triassic Keuper facies) and hydrocarbons are absent in the catchment of the cave. The most plausible explanation for the presence of dissolved sulfate in Devaux's water is the oxidation of pyrite present in the limestone ([du Cailar and Dubois, 1953](#); [Requirand, 2014](#)).

$\delta^{34}\text{S}$ values of gypsum (-11.9 to -15.8 ‰), pyrite (-12.7 ‰), and dissolved sulfate (-14.4 ‰ in dripwater and -28.5 to -27.3 ‰ in Brulle spring water) are within the range of biogenic pyrite and differ notably from values of marine evaporites (10-35 ‰) ([Seal, 2006](#)). Thus, the $\delta^{34}\text{S}$ values together with the geological setting of the cave support the hypothesis that disseminated pyrite in the host limestone is the main source of dissolved sulfate and subsequently of CCG. Only the dissolved sulfate $\delta^{34}\text{S}$ values of Brulle spring are considerably more negative (-28.5‰ and -27.3‰). This may be a consequence of microbially mediated redox processes in the karst that discriminate against ^{34}S ([Zerkle et al., 2016](#); [Temovski et al., 2018](#)). Further studies on the microbiology of the cave may shed light on these mechanisms and how the local sulfur cycle may have changed in the recent past.

In gypsum caves, dissolved sulfate dominates over the bicarbonate, and the typical crystallization sequence during freezing of water with high TDS is gypsum → carbonate (commonly calcite) → celestine ([Žák et al., 2018](#)). In Devaux cave, however, bicarbonate dominates over sulfate, and our observations show that gypsum crystals partly nucleated on CCC_{coarse}. Accordingly, the crystallization sequence at Devaux cave is calcite → gypsum, taking place in a semi-closed system at low freezing rates.

The second aspect that makes the CCG in Devaux cave unique is the size and euhedral shapes of the crystals (Fig. 9 b), which differ notably from the much smaller sizes of gypsum crystals (20-200 μm) and gypsum powders (1-30 μm) found in gypsum caves in Russia and Ukraine ([Žák et al., 2018](#) and references therein). Another characteristic of CCC and CCG occurrences in Devaux cave is the presence of milky ice surrounding them (Fig. 9a, e) which seems to be related

to the freezing process during the formation cryogenic minerals in a subaqueous environment.

Finally, the presence of gypsum aggregates overgrowing blocks (Fig. 9c) supports the hypothesis of subaqueous gypsum formation. On the other hand, the absence of gypsum growing on the ceiling or on the walls allows to discard its formation from seepage water followed by precipitation due to evaporation in the cave (e.g., [Gázquez et al., 2017, 2020](#)). In essence, all observations indicate that gypsum precipitated in a semi-closed subaqueous environment and has been preserved from later dissolution by the exceptionally dry environment of this ice cave. Gypsum precipitating from freezing waters has been also documented in the Arctic and the Antarctica ([Losiak et al., 2016](#); [Wollenburg et al., 2018](#)) and has been proposed as a mechanism for gypsum formation on Mars ([Losiak et al., 2016](#)).

6. Conclusions

The investigation of Devaux ice cave, based on cave monitoring, geomorphology, and geochemical analyses, provides exceptional insights into the origin of modern and past mountain permafrost and associated processes and deposits.

- Devaux cave consists of two parts characterised by different thermal regimes: 1) the near-entrance parts and the main gallery showing large temperature fluctuations and cave air temperatures seasonally exceeding 0°C. These passages are influenced by advective air flow and heat released by the cave river. 2) The inner sector and isolated chambers are characterized by muted thermal oscillations and temperatures constantly below 0°C. There, the cave air temperature is mainly controlled by heat conduction through the bedrock.

- Devaux cave is impacted by backflooding in late winter/early spring when the main outlets freeze, damming the water inside the cave forming a lake. The blocking of the outlets requires temperatures below 0°C in the Gavarnie cirque, while on the southern side of the Monte Perdido massif, temperatures above 0°C allow water infiltration.

- The absence of dripwater in most parts of the cave together with the presence of perennial/seasonal hoarfrost, and the location of massive ice bodies on the ceiling and/or filling cupulas and galleries are indicative of frozen bedrock surrounding the cave. Permafrost at Devaux cave is attributed to a combination of rock undercooling by cave air ventilation and the local climate setting giving rise to the development and/or preservation of permafrost inherited from past colder periods. Currently, permafrost seems to be present above the cave reaching a maximum thickness of ~200 m and a lateral extension of ~350 m towards the southern face of the Monte Perdido massif.

- We report the first deposits of cryogenic gypsum in a limestone-hosted ice cave. Most of the cryogenic minerals are still within the ice and surrounded by milky ice rich in air inclusions. Gypsum precipitation occurred subaqueously as a result of slow freezing, following CCC formation. $\delta^{34}\text{S}$ values show that the sulfate originated from the oxidation of pyrite present in the limestone.

- Current climate conditions seem to be still favourable for the preservation of ice within this cave. This situation contrasts to the large ice mass loss in other ice caves elsewhere. The ice deposits in Devaux cave allow unique insights into processes leading to the formation of cryogenic carbonates and sulfates, and represents a unique site to better understand the mountain permafrost evolution in the Monte Perdido massif and the Pyrenees in general.

Competing interests

No competing of interest

Authors contribution

MB conceived the project, planned fieldwork and the sampling strategy. AM obtained funding for this work. MB and GC installed and maintained the sensors and performed the fieldwork. GC contributed with cave monitoring data from 2011 to 2015. MB analysed monitoring, geomorphological, and geochemical data. FG performed $\delta^{34}\text{S}$ analyses using the facilities provided by AVT. JILM created the radiation map. MB designed the figures and wrote a first draft of the manuscript. ML and CS contributed to the discussion of the data. ML and AM reviewed all versions of the manuscript. All authors reviewed the manuscript and contributed

to the results, discussion, and final interpretation. All authors approved its submission.

Acknowledgements

We thank the directorates of the Parc National des Pyrénées (France) and the Ordesa y Monte Perdido National Park (Spain) for their permission to investigate Devaux cave. We want to especially thank Marc Galy for his cave survey which improves noticeably previously published surveys and for the historical photo of 1984. Also, we thank Météo France for providing climate data from the Pic du midi de Bigorre station. We thank Maria Leunda for a critical review and suggestions to the first draft of the manuscript. We also thank Jerome Labat (SSPPO), Claude Novoa, Alvaro Palacios, Maria Leunda, José Leunda, David Serrano, the Góriz hut staff (www.goriz.es), and the Palazio family (www.hotelpalazio.com) for their invaluable help during fieldwork. We thank Paul Cluzon for the photo of Fig. 1d, and Claude Requirand for his report about Devaux cave. The authors would like to acknowledge the use of the Servicio General de Apoyo a la Investigación-SAI, University of Zaragoza, and Alberto Barcos (IPE-CSIC) for the chemical water analyses. This study contributes to the work carried out by the DGA research group Procesos Geoambientales y Cambio Global (ref.: E02-20R) and the MERS research group 2017 SGR 1588.

Financial support

This research has been supported by the following projects which were funded by the National Parks Autonomous Agency (OAPN) (OCHESTRA-ref 2552/2020), the Spanish Agencia Estatal de Investigación (AEI-Spain) (PICACHU-ref PID2019-106050RB-I00), (SPYRIT- ref CGL2016-77479-R), the PaleoICE EXPLORA project (ref. CGL2015-72167-EXP) and the Comité régional de spéléologie de Nouvelle Aquitaine. Miguel Bartolomé was supported by a postdoctoral fellowship of the Juan de la Cierva-Formación program provided by the Spanish Ministry of Science (ref.: FJCI-2017-31725) and OCHESTRA-ref 2552/2020. Fernando Gázquez was financially supported by a Ramón y Cajal Fellowship (RYC2020-029811-I) of the Spanish Government (Ministerio de Economía y Competividad).

References

- Badino, G., 2010. UNDERGROUND METEOROLOGY-“What’s the weather underground?” *Acta Carsologica* 39. <https://doi.org/10.3986/ac.v39i3.74>
- Bartolomé, M., Sancho, C., Benito, G., Medialdea, A., Calle, M., Moreno, A., Leunda, M., Luetscher, M., Muñoz, A., Bastida, J., Cheng, H., Edwards, R.L., 2021. Effects of glaciation on karst hydrology and sedimentology during the Last Glacial Cycle: The case of Granito cave, Central Pyrenees (Spain). *CATENA* 206, 105252. <https://doi.org/10.1016/j.catena.2021.105252>
- Bartolomé, M., Sancho, C., Osácar, M.C., Moreno, A., Leunda, M., Spötl, C., Luetscher, M., López-Martínez, J., Belmonte, A., 2015. Characteristics of cryogenic carbonates in a Pyrenean ice cave (northern Spain). *Geogaceta* 58 107–110.
- Belmonte-Ribas, Á., Sancho, C., Moreno, A., Lopez-Martinez, J., Bartolome, M., 2014. Present-day environmental dynamics in ice cave a294, central pyrenees, spain. *Geogr. Fis. E Din. Quat.* 37, 131–140. <https://doi.org/10.4461/GFDQ.2014.37.12>
- Biskaborn, B.K., Smith, S.L., Noetzli, J., Matthes, H., Vieira, G., Streletskiy, D.A., Schoeneich, P., Romanovsky, V.E., Lewkowicz, A.G., Abramov, A., Allard, M., Boike, J., Cable, W.L., Christiansen, H.H., Delaloye, R., Diekmann, B., Drozdov, D., Etzel Müller, B., Grosse, G., Guglielmin, M., Ingeman-Nielsen, T., Isaksen, K., Ishikawa, M., Johansson, M., Johansson, H., Joo, A., Kaverin, D., Kholodov, A., Konstantinov, P., Kröger, T., Lambiel, C., Lanckman, J.-P., Luo, D., Malkova, G., Meiklejohn, I., Moskalenko, N., Oliva, M., Phillips, M., Ramos, M., Sannel, A.B.K., Sergeev, D., Seybold, C., Skryabin, P., Vasiliev, A., Wu, Q., Yoshikawa, K., Zheleznyak, M., Lantuit, H., 2019. Permafrost is warming at a global scale. *Nat. Commun.* 10, 264. <https://doi.org/10.1038/s41467-018-08240-4>
- Boeckli, L., Brenning, A., Gruber, S., Noetzli, J., 2012. A statistical approach to modelling permafrost distribution in the European Alps or similar mountain ranges. *The Cryosphere* 6, 125–140. <https://doi.org/10.5194/tc-6-125-2012>
- Bottrell, S.H., 1991. Sulphur isotope evidence for the origin of cave evaporites in Ogof y Daren Cilau, south Wales. *Mineral. Mag.* 55, 209–210. <https://doi.org/10.1180/minmag.1991.055.379.09>
- Bücher, A., Dessens, J., 1991. Secular Trend of Surface Temperature at an Elevated Observatory in the Pyrenees. *J. Clim.* 4, 859–868. [https://doi.org/10.1175/1520-0442\(1991\)004<0859:STOSTA>2.0.CO;2](https://doi.org/10.1175/1520-0442(1991)004<0859:STOSTA>2.0.CO;2)
- Casteret, N., 1953. Dans les glaces souterraines. Les plus élevés de Monde. Librairie Académique Perrin, Paris, p. 93.
- Colucci, R., Luetscher, M., Forteet, E., Guglielmin, M., Lenaz, D., Princivale, F., Vita, F., 2017. First alpine evidence of in situ coarse cryogenic cave carbonates (CCCcoarse). *Geogr. Fis. E Din. Quat.* 53–59. <https://doi.org/10.4461/GFDQ.2017.40.5>
- Colucci, R.R., Guglielmin, M., 2019. Climate change and rapid ice melt: Suggestions from abrupt permafrost degradation and ice melting in an alpine ice cave. *Prog. Phys. Geogr. Earth Environ.* 0309133319846056. <https://doi.org/10.1177/0309133319846056>
- Dessens, J., Bücher, A., 1995. Changes in minimum and maximum temperatures at the Pic du Midi in relation with humidity and cloudiness, 1882–1984. *Atmospheric Res.*, 37, 147–162. [https://doi.org/10.1016/0169-8095\(94\)00075-O](https://doi.org/10.1016/0169-8095(94)00075-O)
- Devaux, J., 1929. Nouvelle grotte Marboréenne. *La Natura* 102–107.
- Devaux, J., 1933. La grotte des sœurs de la cascade. *Études glaciologiques, 1920-1930. Tome VII*, pp. 233-238. Plan & coupe. Paris. Imprimerie Nationale. Ministère de l'Agriculture. Direction des eaux et du génie rural.
- du Cailar, J., Couderc, J., Dubois, P., 1953. La source du Gave de Pau. *Annales de Spéléologie* 181–203.

- du Cailar, J., Dubois, P., 1953. Sur quelques modalités de formation et d'évolution des dépôts cristallins dans les cavités de haute altitude. In: Premier congrès international de spéléologie. Paris, Tome II, pp 325-333.
- Dublyansky, Y., Moseley, G.E., Lyakhnitsky, Y., Cheng, H., Edwards, L.R., Scholz, D., Koltai, G., Spötl, C., 2018. Late Palaeolithic cave art and permafrost in the Southern Ural. *Sci. Rep.* 8, 12080. <https://doi.org/10.1038/s41598-018-30049-w>
- Fankhauser, A., McDermott, F., Fleitmann, D., 2016. Episodic speleothem deposition tracks the terrestrial impact of millennial-scale last glacial climate variability in SW Ireland. *Quat. Sci. Rev.* 152, 104–117. <https://doi.org/10.1016/j.quascirev.2016.09.019>
- Feuillet, T., 2011. Statistical Analyses of Active Patterned Ground Occurrence in the Taillon Massif (Pyrénées, France/Spain). *Permafr. Periglac. Process.* 22, 228–238. <https://doi.org/10.1002/ppp.726>
- García-Ruiz, J.M., Palacios, D., Andrés, N. de, Valero-Garcés, B.L., López-Moreno, J.I., Sanjuán, Y., 2014. Holocene and 'Little Ice Age' glacial activity in the Marboré Cirque, Monte Perdido Massif, Central Spanish Pyrenees. *The Holocene* 24, 1439–1452. <https://doi.org/10.1177/0959683614544053>
- García-Ruiz, J.M., Palacios, D., Andrés, N., López-Moreno, J.I., 2020. Neoglaciation in the Spanish Pyrenees: a multiproxy challenge. *Mediterr. Geosci. Rev.* 2, 21–36. <https://doi.org/10.1007/s42990-020-00022-9>
- Gázquez, F., Bauska, T.K., Comas-Bru, L., Ghaleb, B., Calaforra, J.-M., Hodell, D.A., 2020. The potential of gypsum speleothems for paleoclimatology: application to the Iberian Roman Humid Period. *Sci. Rep.* 10, 14705. <https://doi.org/10.1038/s41598-020-71679-3>
- Gázquez, F., Calaforra, J.M., Evans, N.P., Hodell, D.A., 2017. Using stable isotopes ($\delta^{17}\text{O}$, $\delta^{18}\text{O}$ and δD) of gypsum hydration water to ascertain the role of water condensation in the formation of subaerial gypsum speleothems. *Chem. Geol.* 452, 34–46. <https://doi.org/10.1016/j.chemgeo.2017.01.021>
- Gellatly, A.F., Grove, J.M., Switsur, V.R., 1992. Mid-Holocene glacial activity in the Pyrenees. *The Holocene* 2, 266–270. <https://doi.org/10.1177/095968369200200309>
- Giesemann, A., Jaeger, H.-J., Norman, A.L., Krouse, H.R., Brand, W.A., 1994. Online Sulfur-Isotope Determination Using an Elemental Analyzer Coupled to a Mass Spectrometer. *Anal. Chem.* 66, 2816–2819. <https://doi.org/10.1021/ac00090a005>
- Gomez Lende, M., Berenguer, F., Serrano, E., 2014. Morphology, ice types and thermal regime in a high mountain ice cave. First studies applying terrestrial laser scanner in the Peña Castil ice cave (Picos de Europa, Northern Spain). *Geogr. Fis. E Din. Quat.* 37, 141–150. <https://doi.org/10.4461/GFDQ.2014.37.13>
- Gómez Lende, M., Serrano, E., Bordehore, L.J., Sandoval, S., 2016. The role of GPR techniques in determining ice cave properties: Peña Castil ice cave, Picos de Europa. *Earth Surf. Process. Landf.* 41, 2177–2190. <https://doi.org/10.1002/esp.3976>
- Gómez-Ortiz, A., Oliva, M., Salvador-Franch, F., Palacios, D., Tanarro, L.M., de Sanjosé-Blasco, J.J., Salvà-Catarineu, M., 2019. Monitoring permafrost and periglacial processes in Sierra Nevada (Spain) from 2001 to 2016. *Permafr. Periglac. Process.* 30, 278–291. <https://doi.org/10.1002/ppp.2002>
- González Trueba, J.J., Moreno, R.M., Martínez de Pisón, E., Serrano, E., 2008. 'Little Ice Age' glaciation and current glaciers in the Iberian Peninsula. *The Holocene* 18, 551–568. <https://doi.org/10.1177/0959683608089209>
- Gruber, S., Haeberli, W., 2009. Mountain Permafrost, in: Margesin, R. (Ed.), *Permafrost Soils, Soil Biology*. Springer, Berlin, Heidelberg, pp. 33–44. https://doi.org/10.1007/978-3-540-69371-0_3
- Gubler, S., Fiddes, J., Keller, M., Gruber, S., 2011. Scale-dependent measurement and analysis of ground surface temperature variability in alpine terrain. *The Cryosphere* 5, 431–443. <https://doi.org/10.5194/tc-5-431-2011>

- Haeberli, W., Rellstab, W., Harrison, W.D., 1984. Geothermal Effects of 18 ka BP Ice Conditions in the Swiss Plateau. *Ann. Glaciol.* 5, 56–60. <https://doi.org/10.3189/1984AoG5-1-56-60>
- Harris, C., Vonder Mühll, D., Isaksen, K., Haeberli, W., Sollid, J.L., King, L., Holmlund, P., Dramis, F., Guglielmin, M., Palacios, D., 2003. Warming permafrost in European mountains. *Glob. Planet. Change* 39, 215–225. <https://doi.org/10.1016/j.gloplacha.2003.04.001>
- Heeb, B., 2014. The Next Generation of the DistoX Cave Surveying Instrument. *CREG J.*, 88, 5-8.
- Hercman, H., Gąsiorowski, M., Gradziński, M., Kicińska, D., 2010. The First Dating of Cave Ice from the Tatra Mountains, Poland and its Implication to Palaeoclimate Reconstructions. *Geochronometria* 36, 31–38. <https://doi.org/10.2478/v10003-010-0016-2>
- Hill, C.A., 1987. Geology of Carlsbad Cavern and other caves in the Guadalupe Mountains, New Mexico and Texas. *Bull. 117 N. M. Bur. Mines Miner. Resour.*
- Hock, R., Rasul, G., Adler, C., Cáceres, B., Gruber, S., Hirabayashi, Y., Jackson, J., Kääb, A., Kang, S., Kutuzov, S., Milner, A., Molau, U., Morin, S., Orlove, B., Steltzer, H., 2019. High Mountain Areas. In: IPCC Special Report on the Ocean and Cryosphere in a Changing Climate.
- Kern, Z., Bočić, N., Sipos, G., 2018. Radiocarbon-Dated Vegetal Remains from the Cave Ice Deposits of Velebit Mountain, Croatia. *Radiocarbon* 60, 1391–1402. <https://doi.org/10.1017/RDC.2018.108>
- Kern, Z., Perşoiu, A., 2013. Cave ice – the imminent loss of untapped mid-latitude cryospheric palaeoenvironmental archives. *Quat. Sci. Rev.* 67, 1–7. <https://doi.org/10.1016/j.quascirev.2013.01.008>
- Koltai, G., Spötl, C., Cheng, H., 2020. Cryogenic cave carbonates in the Dolomites (Northern Italy): insights into Younger Dryas cooling and seasonal precipitation. *Clim. Past Discuss.* 1–25. <https://doi.org/10.5194/cp-2020-107>
- Korshunov, V.V., Shavrina, E.V., 1998. Gypsum speleothems of freezing origin. *J. Cave Karst Stud.* 60, 146–150.
- Lechleitner, F.A., Mason, A.J., Breitenbach, S.F.M., Vaks, A., Haghipour, N., Henderson, G.M., 2020. Permafrost-related hiatuses in stalagmites: Evaluating the potential for reconstruction of carbon cycle dynamics. *Quat. Geochronol.* 56, 101037. <https://doi.org/10.1016/j.quageo.2019.101037>
- Leunda, M., González-Sampériz, P., Gil-Romera, G., Bartolomé, M., Belmonte-Ribas, Á., Gómez-García, D., Kaltenrieder, P., Rubiales, J.M., Schwörer, C., Tinner, W., Morales-Molino, C., Sancho, C., 2019. Ice cave reveals environmental forcing of long-term Pyrenean tree line dynamics. *J. Ecol.* 107, 814–828. <https://doi.org/10.1111/1365-2745.13077>
- Lewkowicz, A.G., Ednie, M., 2004. Probability mapping of mountain permafrost using the BTS method, Wolf Creek, Yukon Territory, Canada. *Permafr. Periglac. Process.* 15, 67–80. <https://doi.org/10.1002/ppp.480>
- Li, T.-Y., Baker, J.L., Wang, T., Zhang, J., Wu, Y., Li, H.-C., Blyakharchuk, T., Yu, T.-L., Shen, C.-C., Cheng, H., Kong, X.-G., Xie, W.-L., Edwards, R.L., 2021. Early Holocene permafrost retreat in West Siberia amplified by reorganization of westerly wind systems. *Commun. Earth Environ.* 2, 1–11. <https://doi.org/10.1038/s43247-021-00238-z>
- López-Moreno, J.I., Alonso-González, E., Monserrat, O., Del Río, L.M., Otero, J., Lapazaran, J., Luzi, G., Dematteis, N., Serreta, A., Rico, I., Serrano-Cañadas, E., Bartolomé, M., Moreno, A., Buisan, S., Revuelto, J., 2019. Ground-based remote-sensing techniques for diagnosis of the current state and recent evolution of the Monte Perdido Glacier, Spanish Pyrenees. *J. Glaciol.* 65, 85–100. <https://doi.org/10.1017/jog.2018.96>
- López-Moreno, J.I., Revuelto, J., Rico, I., Chueca-Cía, J., Julián, A., Serreta, A., Serrano, E., Vicente-Serrano, S.M., Azorin-Molina, C., Alonso-González, E., García-Ruiz, J.M., 2016. Thinning of the Monte Perdido Glacier in the Spanish Pyrenees since 1981. *The Cryosphere* 10, 681–694. <https://doi.org/10.5194/tc-10-681-2016>

924 Losiak, A., Derkowski, A., Skąła, A., Trzciński, J., 2016. Evaporites on ice: how to form gypsum
 925 on Antarctica and on Martian North polar residual cap? In: 47th Lunar and Planetary
 926 Science Conference. 1972.pdf.
 927 Luetscher, M., Bolius, D., Schwikowski, M., Schotterer, U., Smart, P.L., 2007. Comparison of
 928 techniques for dating of subsurface ice from Monlesi ice cave, Switzerland. *J. Glaciol.*
 929 53, 374–384.
 930 Luetscher, M., Borreguero, M., Moseley, G.E., Spötl, C., Edwards, R.L., 2013. Alpine permafrost
 931 thawing during the Medieval Warm Period identified from cryogenic cave carbonates.
 932 *The Cryosphere* 7, 1073–1081. <https://doi.org/10.5194/tc-7-1073-2013>
 933 Luetscher, M., Jeannin, P.-Y., 2018. Chapter 12 - Ice Caves in Switzerland, in: Perşoiu, A.,
 934 Lauritzen, S.-E. (Eds.), *Ice Caves*. Elsevier, pp. 221–235. [https://doi.org/10.1016/B978-](https://doi.org/10.1016/B978-0-12-811739-2.00010-3)
 935 [0-12-811739-2.00010-3](https://doi.org/10.1016/B978-0-12-811739-2.00010-3)
 936 Luetscher, M., Lismonde, B., Jeannin, P.-Y., 2008. Heat exchanges in the heterothermic zone of
 937 a karst system: Monlesi cave, Swiss Jura Mountains. *J. Geophys. Res. Earth Surf.* 113.
 938 <https://doi.org/10.1029/2007JF000892>
 939 Lundberg, J., McFarlane, D.A., 2007. Pleistocene depositional history in a periglacial terrane: A
 940 500 k.y. record from Kents Cavern, Devon, United Kingdom. *Geosphere* 3, 199–219.
 941 <https://doi.org/10.1130/GES00085.1>
 942 Marshall, P., Brown, M.C., 1974. Ice in Coulthard Cave, Alberta. *Can. J. Earth Sci.*
 943 <https://doi.org/10.1139/e74-045>
 944 Mavlyudov, B.R., 2008. Caves Glaciation in the Past. Федеральное государственное
 945 бюджетное учреждение науки Институт географии Российской академии наук, pp.
 946 499–505.
 947 Moseley, G.E., Edwards, R.L., Lord, N.S., Spötl, C., Cheng, H., 2021. Speleothem record of mild
 948 and wet mid-Pleistocene climate in northeast Greenland. *Sci. Adv.* 7, eabe1260.
 949 <https://doi.org/10.1126/sciadv.abe1260>
 950 Munroe, J., Kimble, K., Spötl, C., Marks, G.S., McGee, D., Herron, D., 2021. Cryogenic cave
 951 carbonate and implications for thawing permafrost at Winter Wonderland Cave, Utah,
 952 USA. *Sci. Rep.* 11, 6430. <https://doi.org/10.1038/s41598-021-85658-9>
 953 Munroe, J.S., 2021. First investigation of perennial ice in Winter Wonderland Cave, Uinta
 954 Mountains, Utah, USA. *The Cryosphere* 15, 863–881. [https://doi.org/10.5194/tc-15-](https://doi.org/10.5194/tc-15-863-2021)
 955 [863-2021](https://doi.org/10.5194/tc-15-863-2021)
 956 Navarro-Serrano, F., López-Moreno, J.I., Azorin-Molina, C., Alonso-González, E., Tomás-
 957 Burguera, M., Sanmiguel-Valladolid, A., Revuelto, J., Vicente-Serrano, S.M., 2018.
 958 Estimation of near-surface air temperature lapse rates over continental Spain and its
 959 mountain areas. *Int. J. Climatol.* 38, 3233–3249. <https://doi.org/10.1002/joc.5497>
 960 Noetzli, J., Gruber, S., 2009. Transient thermal effects in Alpine permafrost. *The Cryosphere* 3,
 961 85–99. <https://doi.org/10.5194/tc-3-85-2009>
 962 Orvošová, M., Deininger, M., Milovský, R., 2014. Permafrost occurrence during the Last
 963 Permafrost Maximum in the Western Carpathian Mountains of Slovakia as inferred
 964 from cryogenic cave carbonate. *Boreas* 43, 750–758.
 965 <https://doi.org/10.1111/bor.12042>
 966 Perşoiu, A., Buzjak, N., Onaca, A., Pennos, C., Sotiriadis, Y., Ionita, M., Zachariadis, S., Styllas,
 967 M., Kosutnik, J., Hegyi, A., Butorac, V., 2021. Record summer rains in 2019 led to
 968 massive loss of surface and cave ice in SE Europe. *The Cryosphere* 15, 2383–2399.
 969 <https://doi.org/10.5194/tc-15-2383-2021>
 970 Perşoiu, A., Lauritzen, S.-E. (Eds.), 2018. *Ice caves*. Elsevier, Amsterdam, Netherlands.
 971 Perşoiu, A., Onac, B.P., Wynn, J.G., Blaauw, M., Ionita, M., Hansson, M., 2017. Holocene winter
 972 climate variability in Central and Eastern Europe. *Sci. Rep.* 7, 1196.
 973 <https://doi.org/10.1038/s41598-017-01397-w>

- Pons, X., Ninyerola, M., 2008. Mapping a topographic global solar radiation model implemented in a GIS and refined with ground data. *Int. J. Climatol.* 28, 1821–1834. <https://doi.org/10.1002/joc.1676>
- Racine, T.M.F., Spötl, C., Reimer, P.J., Čarga, J., 2022. RADIOCARBON CONSTRAINTS ON PERIODS OF POSITIVE CAVE ICE MASS BALANCE DURING THE LAST MILLENNIUM, JULIAN ALPS (NW SLOVENIA). *Radiocarbon* 1–24. <https://doi.org/10.1017/RDC.2022.26>
- Reille, M., Andrieu, V., 1995. The late Pleistocene and Holocene in the Lourdes Basin, Western Pyrénées, France: new pollen analytical and chronological data. *Veg. Hist. Archaeobotany* 4, 1–21. <https://doi.org/10.1007/BF00198611>
- Requirand, C., 2014. Hypothèse sur la formation des cristaux de gypse Grotte Glacée Devaux (Gavarnie - Hautes Pyrénées). *Bulletin de la Société Ramon.* 11 pp.
- Richter, D.K., Meissner, P., Immenhauser, A., Schulte, U., Dorsten, I., 2010a. Cryogenic and non-cryogenic pool calcites indicating permafrost and non-permafrost periods: a case study from the Herbstlabyrinth-Advent Cave system (Germany). *The Cryosphere* 4, 501–509. <https://doi.org/10.5194/tc-4-501-2010>
- Richter, D.K., Meissner, P., Immenhauser, A., Schulte, U., Dorsten, I., 2010b. Cryogenic and non-cryogenic pool calcites indicating permafrost and non-permafrost periods: a case study from the Herbstlabyrinth-Advent Cave system (Germany). *The Cryosphere* 4, 501–509. <https://doi.org/10.5194/tc-4-501-2010>
- Rico, I., Magnin, F., López Moreno, J.I., Serrano, E., Alonso-González, E., Revuelto, J., Hughes-Allen, L., Gómez-Lende, M., 2021. First evidence of rock wall permafrost in the Pyrenees (Vignemale peak, 3,298 m a.s.l., 42°46′16″N/0°08′33″W). *Permafr. Periglac. Process.* 32, 673–680. <https://doi.org/10.1002/ppp.2130>
- Rodríguez-Salgado, P., Oms, O., Ibáñez-Insa, J., Anadón, P., Gómez de Soler, B., Campeny, G., Agustí, J., 2021. Mineralogical proxies of a Pliocene maar lake recording changes in precipitation at the Camp dels Ninots (Pliocene, NE Iberia). *Sediment. Geol.* 418, 105910. <https://doi.org/10.1016/j.sedgeo.2021.105910>
- Rösch, G., Rösch, J., 1935. Visites à la grotte Devaux. *La Montagne. Revue du Club Alpin Français*, N° 269, pp.171-178.
- Rösch, J., 1949. Une exploration de la Grotte Devaux à Gavarnie. *Bulletin de la section du Sud-Ouest de la Club Alpin Français*, N°69. pp. 103-107.
- Sancho, C., Arenas, C., Pardo, G., Peña-Monné, J.L., Rhodes, E.J., Bartolomé, M., García-Ruiz, J.M., Martí-Bono, C., 2018a. Glaciolacustrine deposits formed in an ice-dammed tributary valley in the south-central Pyrenees: New evidence for late Pleistocene climate. *Sediment. Geol.* 366, 47–66. <https://doi.org/10.1016/j.sedgeo.2018.01.008>
- Sancho, C., Belmonte, Á., Bartolomé, M., Moreno, A., Leunda, M., López-Martínez, J., 2018b. Middle-to-late Holocene palaeoenvironmental reconstruction from the A294 ice-cave record (Central Pyrenees, northern Spain). *Earth Planet. Sci. Lett.* 484, 135–144. <https://doi.org/10.1016/j.epsl.2017.12.027>
- Sancho, C., Peña, J.L., Mikkan, R., Osácar, C., Quinif, Y., 2004. Morphological and speleothemic development in Brujas Cave (Southern Andean Range, Argentina): palaeoenvironmental significance. *Geomorphology* 57, 367–384. [https://doi.org/10.1016/S0169-555X\(03\)00166-1](https://doi.org/10.1016/S0169-555X(03)00166-1)
- Scandroglio, R., Draebing, D., Offer, M., Krautblatter, M., 2021. 4D quantification of alpine permafrost degradation in steep rock walls using a laboratory-calibrated electrical resistivity tomography approach. *Surf. Geophys.* 19, 241–260. <https://doi.org/10.1002/nsg.12149>
- Seal, R.R., II, 2006. Sulfur Isotope Geochemistry of Sulfide Minerals. *Rev. Mineral. Geochem.* 61, 633–677. <https://doi.org/10.2138/rmg.2006.61.12>
- Serrano, E., Gómez-Lende, M., Belmonte, Á., Sancho, C., Sánchez-Benítez, J., Bartolomé, M., Leunda, M., Moreno, A., Hivert, B., 2018. Chapter 28 - Ice Caves in Spain, in: Perşoiu,

- A., Lauritzen, S.-E. (Eds.), *Ice Caves*. Elsevier, pp. 625–655.
<https://doi.org/10.1016/B978-0-12-811739-2.00028-0>
- Serrano, E., López-Moreno, J.I., Gómez-Lende, M., Pisabarro, A., Martín-Moreno, R., Rico, I., Alonso-González, E., 2020. Frozen ground and periglacial processes relationship in temperate high mountains: a case study at Monte Perdido-Tucarroya area (The Pyrenees, Spain). *J. Mt. Sci.* 17, 1013–1031. <https://doi.org/10.1007/s11629-019-5614-5>
- Serrano, E., Sanjosé-Blasco, J.J. de, Gómez-Lende, M., López-Moreno, J.I., Pisabarro, A., Martínez-Fernández, A., 2019. Periglacial environments and frozen ground in the central Pyrenean high mountain area: Ground thermal regime and distribution of landforms and processes. *Permafr. Periglac. Process.* 30, 292–309.
<https://doi.org/10.1002/ppp.2032>
- Spötl, C., Cheng, H., 2014. Holocene climate change, permafrost and cryogenic carbonate formation: insights from a recently deglaciated, high-elevation cave in the Austrian Alps. *Clim. Past* 10, 1349–1362. <https://doi.org/10.5194/cp-10-1349-2014>
- Spötl, C., Koltai, G., Jarosch, A.H., Cheng, H., 2021. Increased autumn and winter precipitation during the Last Glacial Maximum in the European Alps. *Nat. Commun.* 12, 1839.
<https://doi.org/10.1038/s41467-021-22090-7>
- Spötl, C., Reimer, P.J., Luetscher, M., 2014. Long-term mass balance of perennial firn and ice in an Alpine cave (Austria): Constraints from radiocarbon-dated wood fragments. *The Holocene* 0959683613515729. <https://doi.org/10.1177/0959683613515729>
- Stoffel, M., Luetscher, M., Bollschweiler, M., Schlatter, F., 2009. Evidence of NAO control on subsurface ice accumulation in a 1200 yr old cave-ice sequence, St. Livres ice cave, Switzerland. *Quat. Res.* 72, 16–26. <https://doi.org/10.1016/j.yqres.2009.03.002>
- Supper, R., Ottowitz, D., Jochum, B., Römer, A., Pfeiler, S., Kauer, S., Keuschnig, M., Ita, A., 2014. Geoelectrical monitoring of frozen ground and permafrost in alpine areas: field studies and considerations towards an improved measuring technology. *Surf. Geophys.* 12, 93–115. <https://doi.org/10.3997/1873-0604.2013057>
- Temovski, M., Futó, I., Túri, M., Palcsu, L., 2018. Sulfur and oxygen isotopes in the gypsum deposits of the Provalata sulfuric acid cave (Macedonia). *Geomorphology* 315, 80–90.
<https://doi.org/10.1016/j.geomorph.2018.05.010>
- Vaks, A., Gutareva, O.S., Breitenbach, S.F.M., Avirmed, E., Mason, A.J., Thomas, A.L., Osinzev, A.V., Kononov, A.M., Henderson, G.M., 2013. Speleothems Reveal 500,000-Year History of Siberian Permafrost. *Science* 340, 183–186.
<https://doi.org/10.1126/science.1228729>
- Vaks, A., Mason, A.J., Breitenbach, S.F.M., Kononov, A.M., Osinzev, A.V., Rosensaft, M., Borshevsky, A., Gutareva, O.S., Henderson, G.M., 2020. Palaeoclimate evidence of vulnerable permafrost during times of low sea ice. *Nature* 577, 221–225.
<https://doi.org/10.1038/s41586-019-1880-1>
- Wind, M., Obleitner, F., Racine, T., Spötl, C., 2022. Multi-annual temperature evolution and implications for cave ice development in a sag-type ice cave in the Austrian Alps. *Cryosphere Discuss.* 1–26. <https://doi.org/10.5194/tc-2022-67>
- Wollenburg, J.E., Katlein, C., Nehrke, G., Nöthig, E.-M., Matthiessen, J., Wolf- Gladrow, D.A., Nikolopoulos, A., Gázquez-Sanchez, F., Rossmann, L., Assmy, P., Babin, M., Bruyant, F., Beaulieu, M., Dybwad, C., Peeken, I., 2018. Ballasting by cryogenic gypsum enhances carbon export in a *Phaeocystis* under-ice bloom. *Sci. Rep.* 8, 7703.
<https://doi.org/10.1038/s41598-018-26016-0>
- Yonge, C.J., Ford, D., Horne, G., Lauriol, B., Schroeder, J., 2018. Chapter 15 - Ice Caves in Canada, in: Perşoiu, A., Lauritzen, S.-E. (Eds.), *Ice Caves*. Elsevier, pp. 285–334.
<https://doi.org/10.1016/B978-0-12-811739-2.00015-2>

1076 Žák, K., Onac, B.P., Kadebskaya, O.I., Filippi, M., Dublyansky, Y., Luetscher, M., 2018. Chapter 6
 1077 - Cryogenic Mineral Formation in Caves, in: Perşoiu, A., Lauritzen, S.-E. (Eds.), Ice
 1078 Caves. Elsevier, pp. 123–162. <https://doi.org/10.1016/B978-0-12-811739-2.00035-8>
 1079 Žák, K., Richter, D.K., Filippi, M., Živor, R., Deininger, M., Mangini, A., Scholz, D., 2012. Coarsely
 1080 crystalline cryogenic cave carbonate – a new archive to estimate the Last
 1081 Glacial minimum permafrost depth in Central Europe. *Clim. Past* 8, 1821–1837.
 1082 <https://doi.org/10.5194/cp-8-1821-2012>
 1083 Žák, K., Urban, J., Čílek, V., Hercman, H., 2004. Cryogenic cave calcite from several Central
 1084 European caves: age, carbon and oxygen isotopes and a genetic model. *Chem. Geol.*
 1085 206, 119–136. <https://doi.org/10.1016/j.chemgeo.2004.01.012>
 1086 Zerkle, A.L., Jones, D.S., Farquhar, J., Macalady, J.L., 2016. Sulfur isotope values in the sulfidic
 1087 Frasassi cave system, central Italy: A case study of a chemolithotrophic S-based
 1088 ecosystem. *Geochim. Cosmochim. Acta* 173, 373–386.
 1089 <https://doi.org/10.1016/j.gca.2015.10.028>

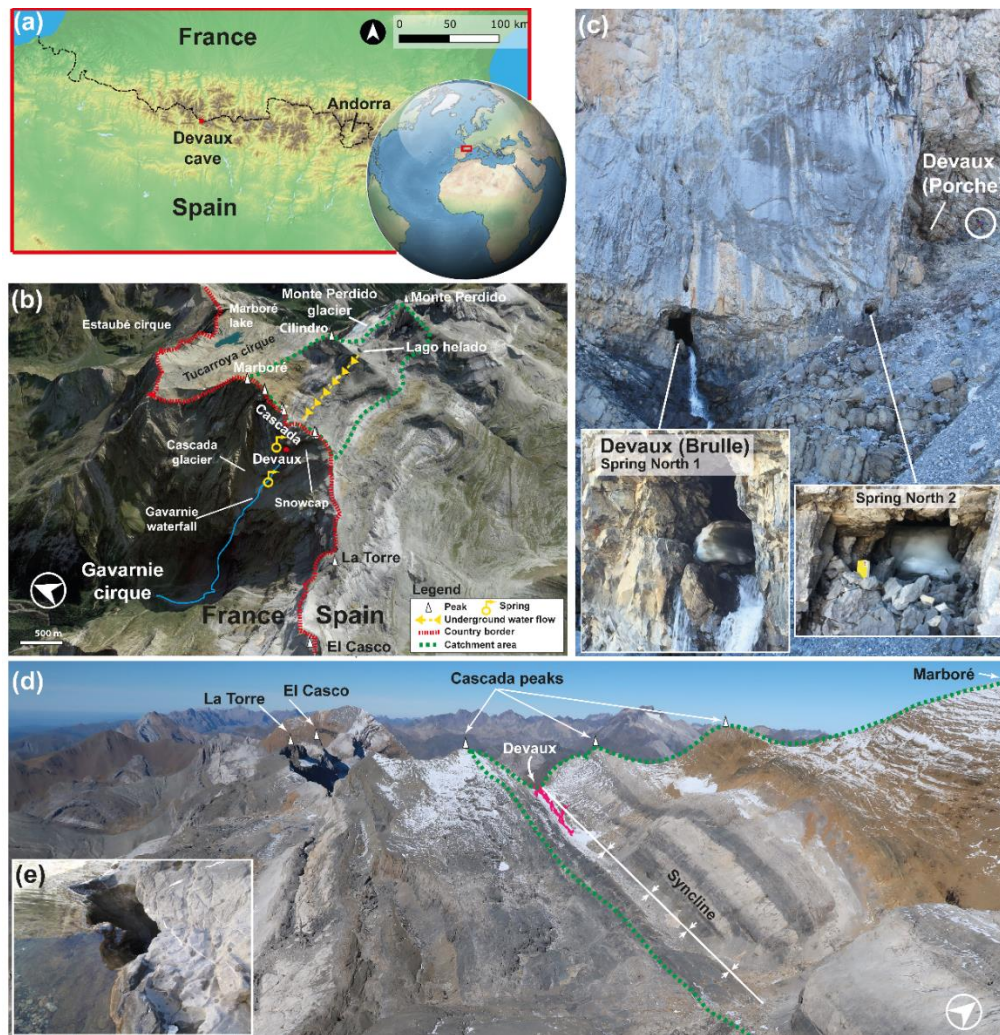


Figure 1. (a) Location of Devaux cave in the Central Pyrenees (ASTER GDEM, NASA v3, 2019). (b) Satellite image and location of Devaux cave, main peaks, lakes, glaciers and cirques in the study area (3D ©Google Earth). The yellow arrows indicate the underground flow path from Lago helado to the Gavarnie waterfall according to the dye-tracing experiment of [du Cailar et al., \(1953\)](#). (c) View towards the entrances of Devaux cave. The lower entrance (~2821 m a.s.l.) corresponds to the Brulle spring (Spring North 1), while the upper one corresponds to the main entrance (Porche (South), ~2836 m a.s.l.). Spring North 2 is located between both entrances. Note person for scale (within the white circle). Remnants of ice partially blocking Brulle and Spring North 2 (July 2021). (d) Landscape view of the catchment area and approximate location of Devaux cave (in dark pink; photo: Paul Cluzon). (e) Ponor located on the southern shore of Lago Helado.

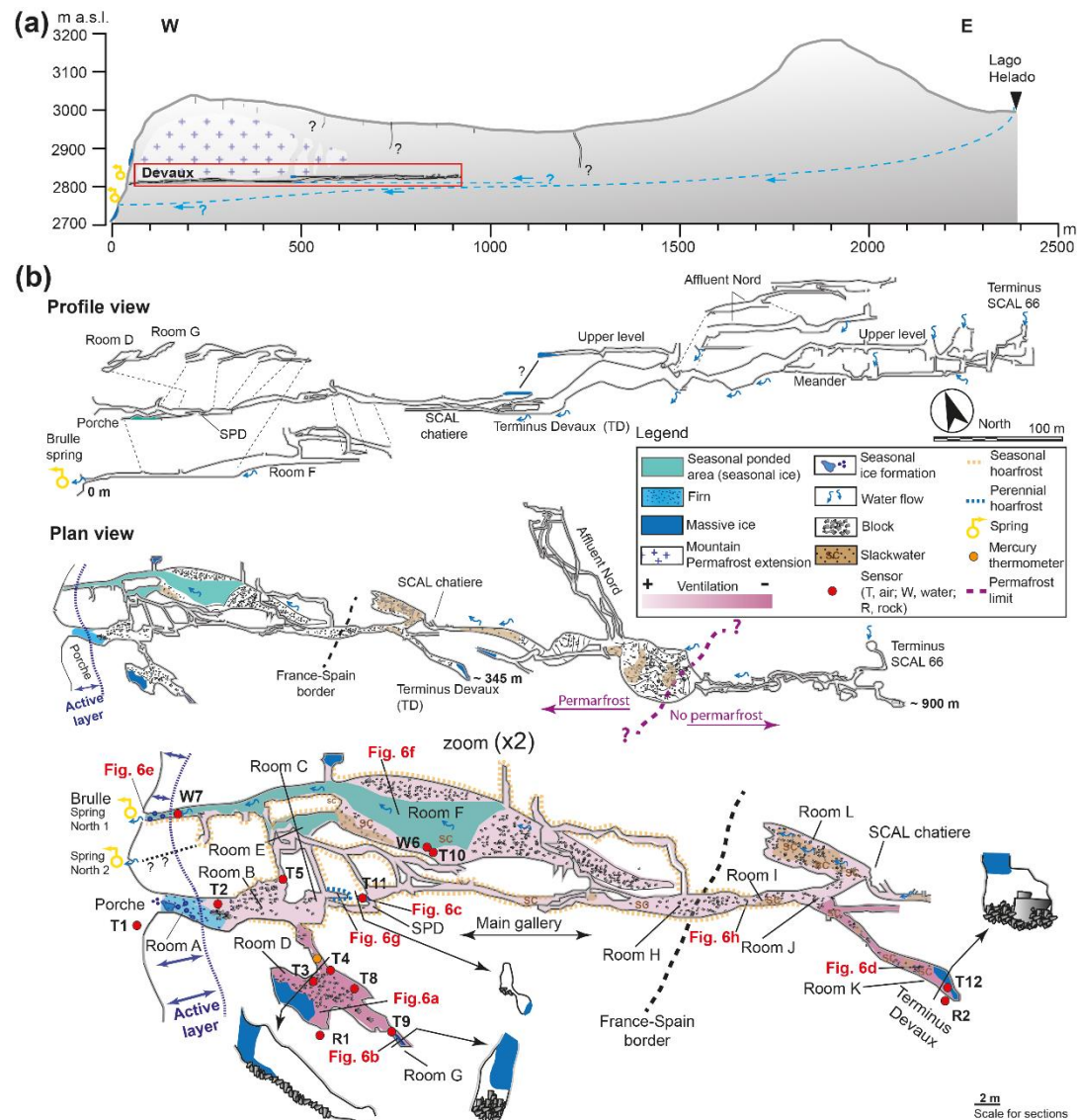


Figure 2. (a) Schematic W-E cross section from Lago helado to Devaux cave, the assumed extent of mountain permafrost, and the interpreted underground flow path according to [du Cailar et al., \(1953\)](#). (b) Longitudinal section and plan view of Devaux cave showing the locations of sensors and cave deposits. Labels R, W and T refer to rock, water and air temperature sensors, respectively. The enlarged area corresponds to the first ~345 m of the studied sector. Red labels correspond to the approximate location of the photographs in Fig. 6. Cave survey by Marc Galy, Groupe Spéléologique des Pyrénées (GSPY 86).

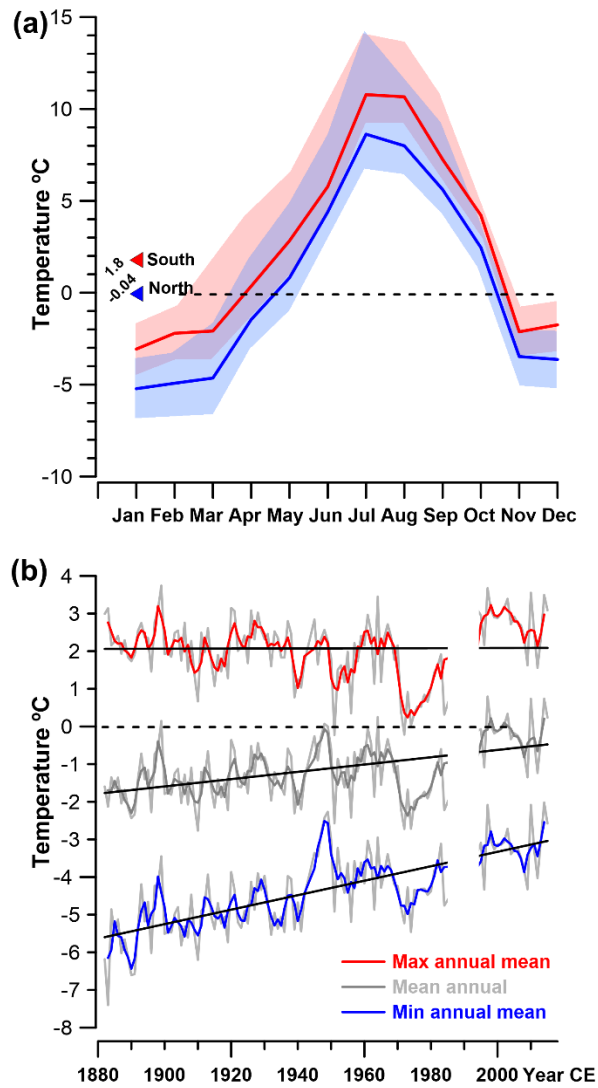


Figure 3. (a) Monthly temperature variation on the northern and southern side of the Monte Perdido massif. Red and blue triangles correspond to the 4-year means. The dashed black line indicates 0°C. Light red and blue shaded envelopes represent the maximum and minimum mean monthly temperatures, respectively. (b) Maximum, mean and minimum annual temperatures recorded at the Pic du Midi de Bigorre station since 1882. Black line indicates the general trend and dashed black line corresponds to 0°C.

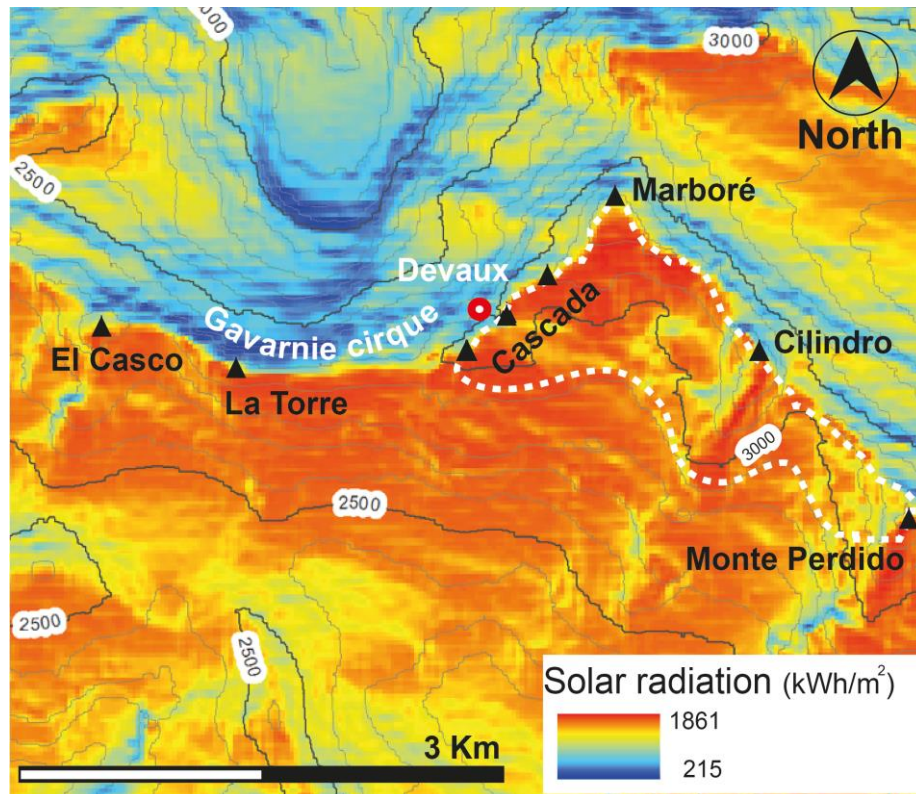


Figure 4. Solar radiation map of the study area. The solar radiation anomaly observed in the Gavarnie cirque is explained by its northerly orientation and the cirque morphology. Black triangles indicate the main peaks above 3000 m. The red-white circle marks Devaux cave, while the dashed white line delineates the approximate catchment.

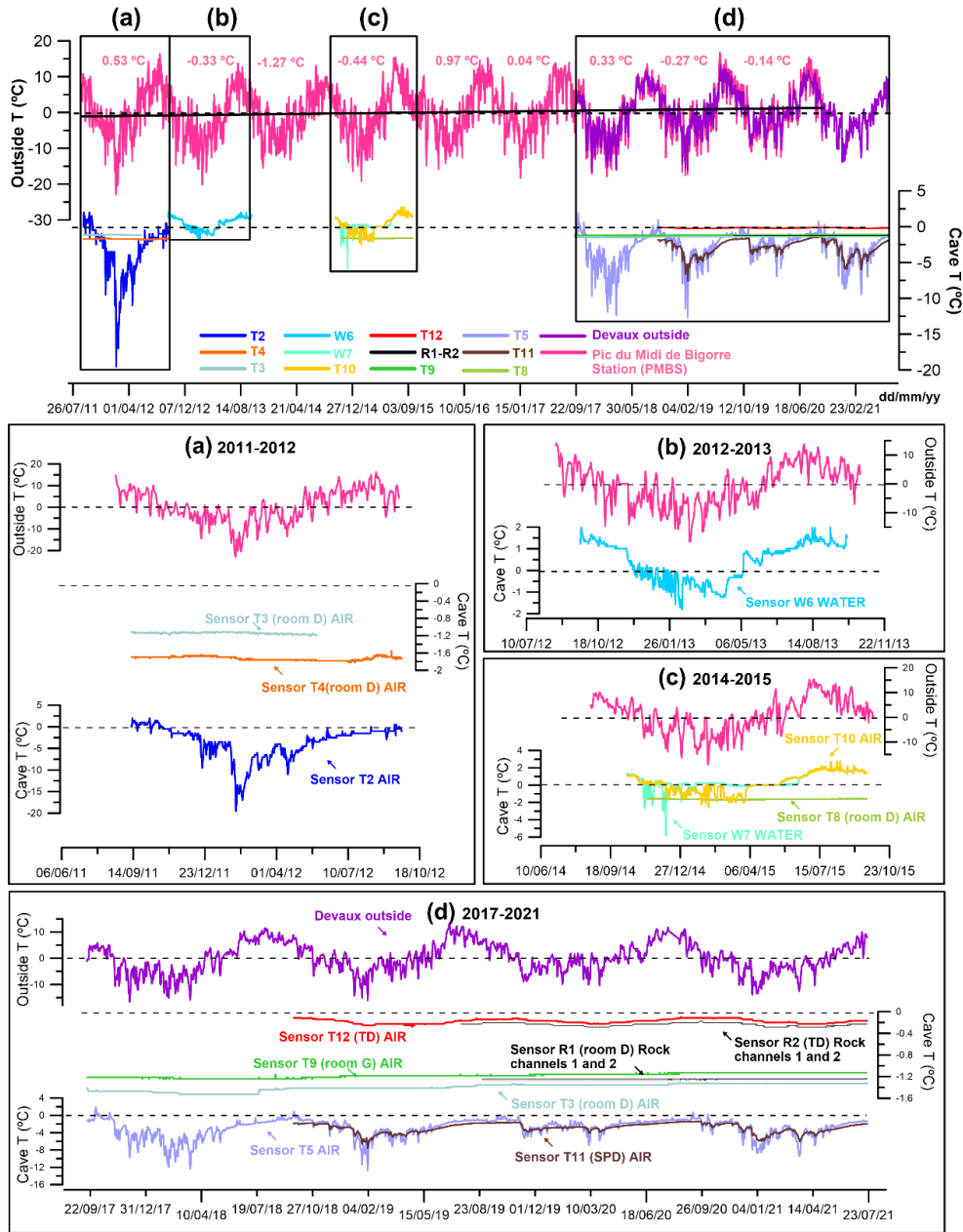


Figure 5. Mean daily air temperature variations at the Pic du Midi de Bigorre station (2860 m a.s.l., red), daily outside air temperature at Devaux cave (2836 m a.s.l., purple) and temperature variations in air, water and rock in the cave for the different time windows since 2011. Dark pink numbers are mean annual air temperatures (MAAT) at the Pic du Midi de Bigorre station (PMBS). Dashed lines indicate 0 °C. Black squares labelled a, b, c, and d correspond to the areas enlarged below. The black continuous line is the external temperature trend during the monitoring period.

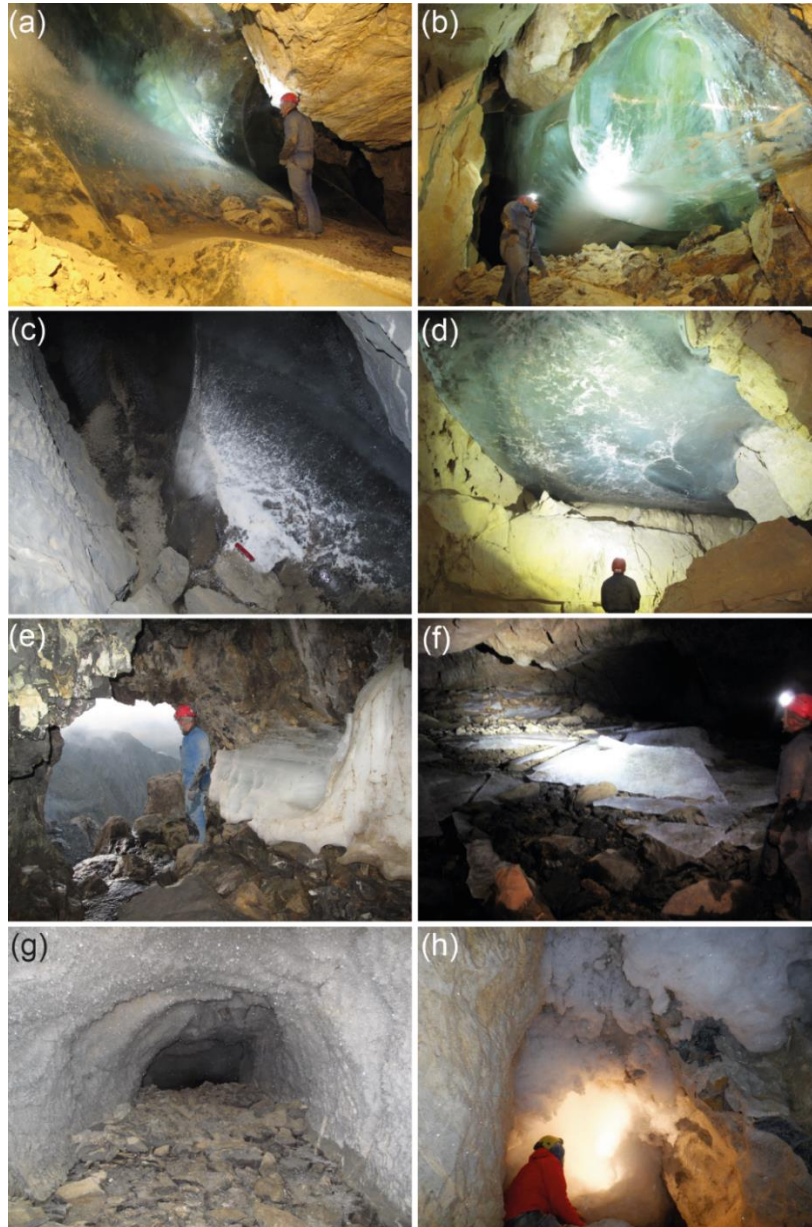


Figure 6. (a) Upper part of the ice body in room D. (b) Ice body hanging from the ceiling and the southwest wall in room G. White spots near the bottom of the deposit correspond to air inclusions as well as cryogenic carbonates and gypsum in the ice. (c) Small ice body in room SPD with CCC-CCG on and within the ice. Red knife (9 cm) for scale. (d) Ice body on the ceiling of room K (Terminus Devaux, TD). (e) Brulle spring and remains of a layered ice body (September 2018). (f) Broken ice sheets in the flooded area in room F (September 2018). (g) Millimetre to centimetre size perennial hoarfrost in a blind gallery below SPD room. (h) Seasonal hoarfrost aggregates (>30 cm long size) covering a cupola close to room J.

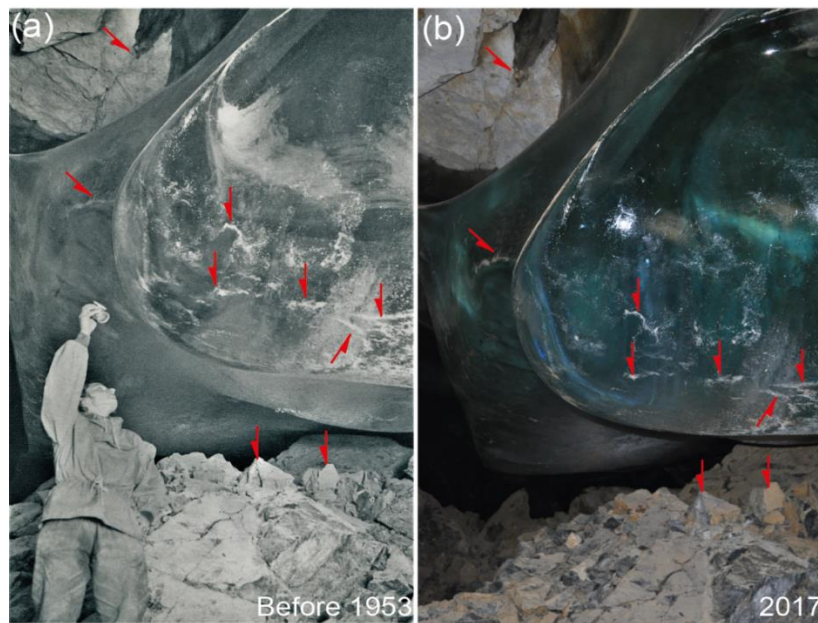


Figure 7. (a) Photo of the ice body located in room G taken shortly before 1953 ([Casteret, 1953](#)). (b) Photo taken in 2017. In both pictures, white patches on the ice surface correspond to small CCC accumulations released from the ice by sublimation. Red arrows indicate common features in both images.

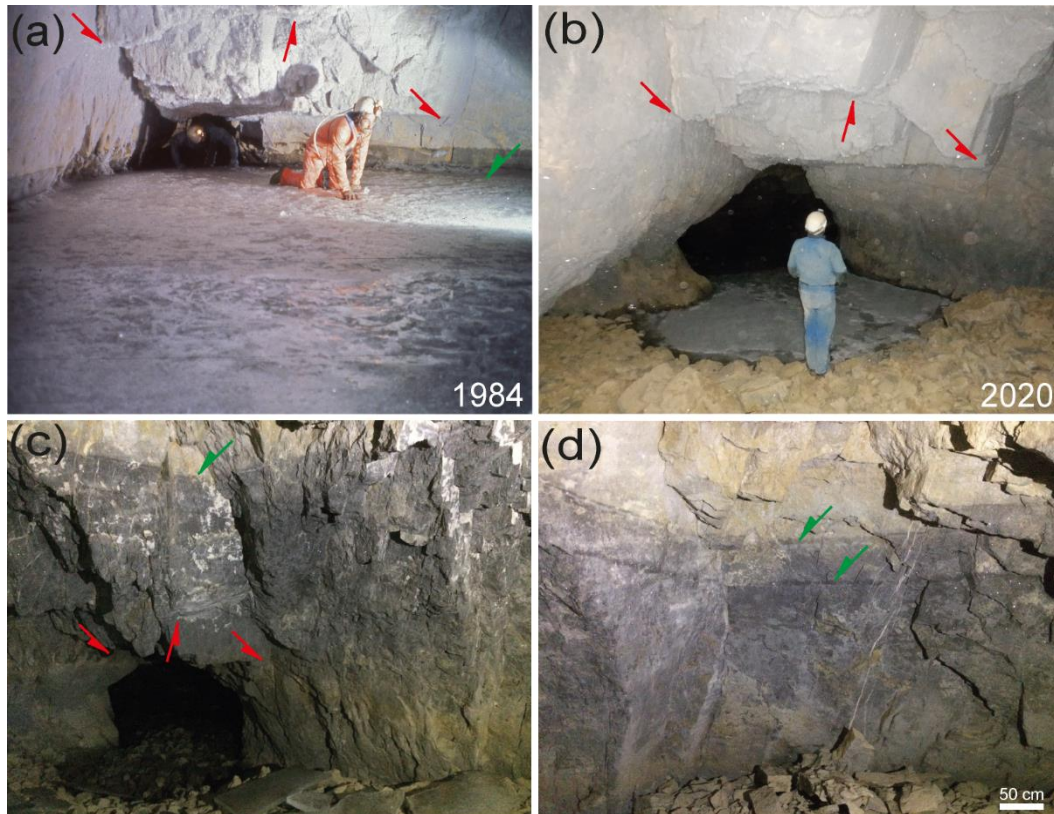


Figure 8. (a) Photo taken close to the river sector that connects the rooms F and E. The estimated ice level is 5 m higher than the Brulle spring. Photo by Jean Luc Bernardin (8th August 1984). (b) Similar area in 2020, and maximum extension of the seasonal lake ice formed during winter. (c) Higher ice mark level (c. +9.5 m with respect to the Brulle spring) and remnants of ice sheets from the frozen lake in 2018. (d) Two ice level marks (c. +9.2 m and +8.8 m with respect to the Brulle spring) located between the highest mark and the elevation of the ice in photo (a). In all images red arrows indicate the same rock edges, while green arrows show ice-level marks.

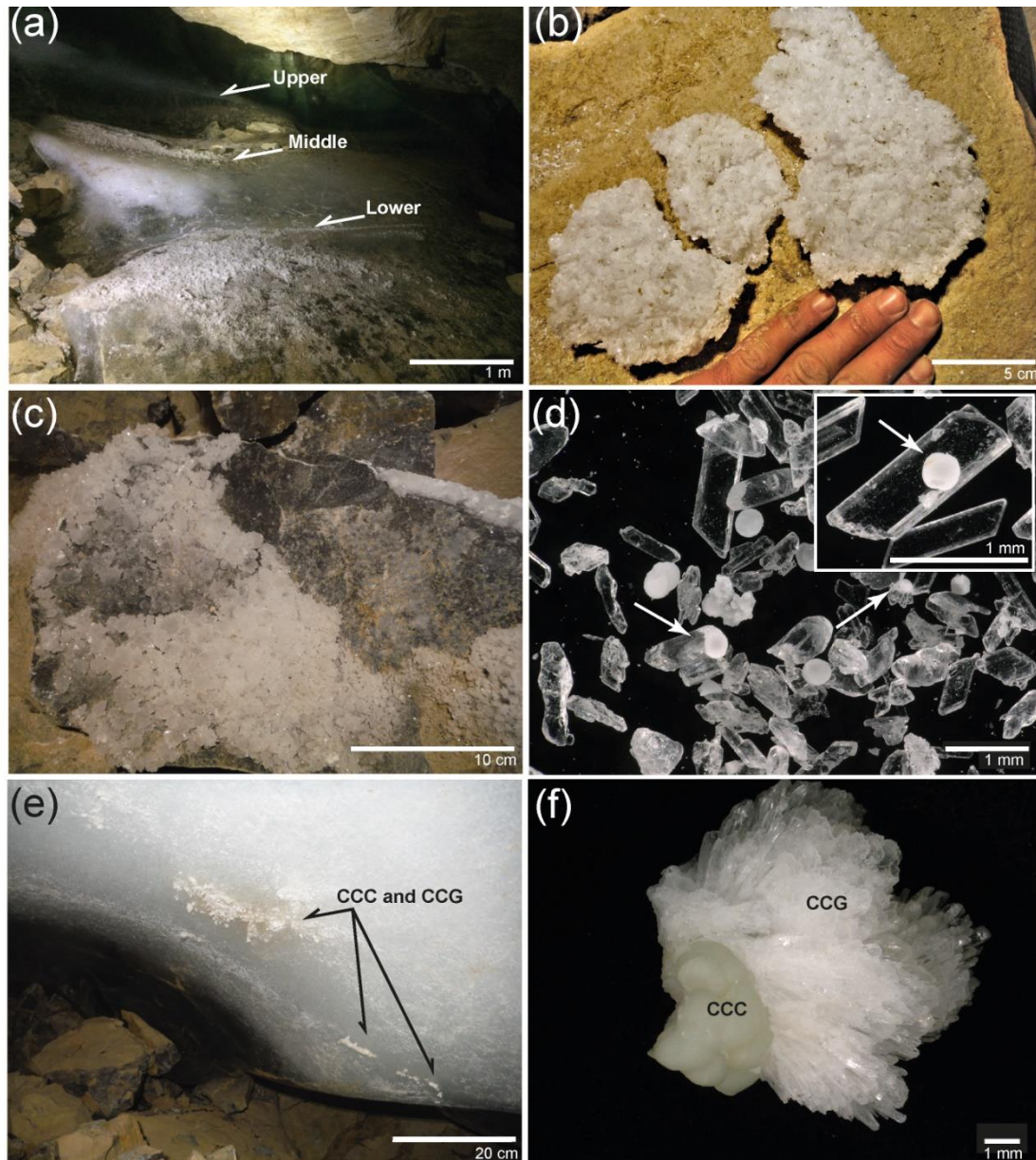


Figure 9. (a) Ice body in room G and three levels marked by cryogenic gypsum partially still in situ in the ice. The white area corresponds to milky ice with a high abundance of air inclusions. Gypsum crystals cover parts of the surface of the ice body due to ice retreat. (b) Large gypsum "raft" deposited on a block in room D. (c) Block in room D with gypsum overgrowths. (d) Microscopic image of euhedral CCG with cores of CCC (white arrows), globular CCC, and enlarged image of euhedral gypsum crystal with a nucleus of globular CCC. (e) CCC and CCG entrapped within milky ice in room G. (f) Detail of a CCC sample from room G covered by CCG.

Date	Sample	Cations					Anions								
		Na ⁺	NH ₄ ⁺	K ⁺	Ca ²⁺	Mg ²⁺	F ⁻	Cl ⁻	NO ₂ ⁻	Br ⁻	NO ₃ ⁻	SO ₄ ²⁻	HCO ₃ ⁻	CO ₃ ²⁻	PO ₄ ³⁻
15/09/2017	Devaux river 1	1.6	0.0	0.5	36.0	8.5	0.0	0.2	0.0	0.0	1.8	21.6	61.0	11.6	0.0
	Devaux drip 1	0.9	0.1	0.5	50.5	18.2	0.1	0.5	0.0	0.0	6.8	67.4	95.2	0.0	0.0
	Devaux drip 2	1.4	1.2	1.3	53.2	19.5	0.1	1.1	0.1	0.0	7.4	70.1	101.3	0.0	0.0
22/07/2018	Devaux Ice 1 (room D)	2.3	0.0	0.3	24.8	2.7	0.1	1.3	0.0	0.0	0.7	19.0	23.9	1.0	0.0
	Devaux Ice 2 (room D)	2.2	1.3	2.5	27.8	2.0	0.0	2.1	0.0	0.0	1.5	17.0	30.7	0.0	0.0
	Devaux river 1	0.6	0.0	0.4	32.4	4.4	0.0	0.2	0.0	0.0	0.9	5.1	53.7	4.0	0.1
22/09/2018	Devaux river 2	0.6	0.0	0.4	32.2	4.4	0.0	0.2	0.0	0.0	0.9	5.1	56.1	2.6	0.0
	Devaux drip 1	1.4	0.0	3.2	61.0	20.8	0.2	2.2	0.0	0.0	14.1	76.0	84.2	5.6	0.0
	Devaux drip 2	2.3	0.1	1.7	60.8	21.0	0.2	2.2	0.0	0.0	14.1	76.9	91.5	4.4	0.0
28/07/2020	Devaux river 1*	1.3	0.0	0.4	40.5	7.9	0.0	0.3	0.0	0.0	2.0	17.0	65.9	0.0	0.0
	Devaux drip 1*	1.6	0.0	1.2	70.6	27.2	0.2	1.1	0.0	0.0	19.8	116.5	90.3	0.0	0.0
	Devaux ice (seasonal)*	0.4	0.0	0.5	28.2	1.1	0.1	0.5	0.0	0.0	0.5	2.8	36.6	0.0	0.0
26/07/2021	Devaux river 1*	0.6	0.0	0.3	31.5	4.1	0.0	0.2	0.0	0.0	0.8	5.9	58.6	0.0	0.0
	Devaux drip 1*	1.1	0.2	1.1	42.3	12.5	0.1	0.5	0.0	0.0	2.9	38.4	101.3	0.0	0.0
	Devaux drip 2*	1.1	0.1	1.0	43.6	13.5	0.1	0.4	0.0	0.0	2.7	38.2	89.1	0.0	0.0
13/08/2021	Devaux drip 3*	1.6	0.7	1.5	47.9	13.1	0.1	1.1	0.0	0.0	2.2	36.7	107.4	0.0	0.0
	Devaux drip 1	2.9	0.0	1.1	83	35.9	0.3	5.9	0.6	0.1	40.2	269.3	104.9	0.0	0.0
	Devaux drip 2	3.3	0.4	2.0	73.2	29.3	0.2	6.0	0.1	0.0	28.6	212	112.2	0.0	0.0
26/07/2021	Devaux river 1	0.4	0.0	0.1	25.7	4.3	0.1	2.6	0.1	0.0	3.2	16.3	68.3	0.0	0.0
	Devaux river 1	0.7	0.0	0.2	28.6	4.9	0.1	2.6	0.0	0.0	1.5	20.4	74.4	0.0	0.0
	Devaux drip 1	7.5	2.2	5.1	49.5	15.2	0.2	10.3	0.3	0.0	6.9	77.3	130.5	0.0	0.0
26/07/2021	Devaux drip 2	5.1	1.3	2.8	49.3	15.6	0.2	6.5	0.1	0.0	6.5	80.5	129.3	0.0	0.0

Table 1. Chemical composition of water and ice samples from Devaux cave (in mg/l). * Samples where TDS (total dissolved solids) was calculated.

Location	Sample and description	$\delta^{34}\text{S}$ (‰) VCDT
Room D	Gypsum crystal (part of large raft)	-15.8
Room D	Gypsum crystal (part of large raft)	-15.5
Room D; lower gypsum level	Gypsum crystal (individual)	-15.6
Room D; middle gypsum level	Gypsum crystal (individual)	-15.0
Room D; middle gypsum level	Gypsum crystal (individual)	-15.6
Room D; upper gypsum level	Tiny gypsum crystals (aliquot)	-15.3
Room D	Gypsum crystal (individual)	-15.1
Room G	Gypsum crystal (individual)	-12.3
Room G	Gypsum overgrowth (individual)	-12.1
Room G	Gypsum overgrowth (individual)	-11.9
Room G	Gypsum overgrowth (individual)	-12.1
Room G	Gypsum overgrowth (individual)	-12.0
Limestone above cave	Pyrite crystal (individual)	-12.7
Entrance "Porche"	Drip water (1 liter)	-14.4
Brulle spring	River water 1 (1 liter)	-28.5
Brulle spring	River water 2 (1 liter)	-27.3

Table 2. Sulfur isotope values of gypsum, water and pyrite from Devaux.